GEOCHRONOLOGY
Open Access
EGU

Navigating the complexity of detrital rutile provenance: methodological insights from the Neotethys Orogen in Anatolia

Megan A. Mueller[1,2,a], **Alexis Licht**[1,3], **Andreas Möller**[4], **Cailey B. Condit**[1], **Julie C. Fosdick**[2], **Faruk Ocakoğlu**[5], and **Clay Campbell**[6]

[1]Department of Earth and Space Sciences, University of Washington, 4000 15th Avenue NE, Seattle, WA 98195, USA
[2]Department of Earth Sciences, University of Connecticut, 354 Mansfield Road – Unit 1045, Storrs, CT 06269, USA
[3]Aix-Marseille Université, CNRS, IRD, INRAE, Collège de France, CEREGE, Technopôle de l'Arbois-Méditerranée, BP80, 13545 Aix-en-Provence, France
[4]Department of Geology, The University of Kansas, 1414 Naismith Drive, Lawrence, KS 66045, USA
[5]Department of Geological Engineering, Eskişehir Osmangazi University, Büyükdere, 26040 Eskişehir, Türkiye
[6]Department of Geosciences, University of Arizona, 1040 E 4th St, Tucson, AZ 85721, USA
[a]now at: Department of Earth and Planetary Sciences, Jackson School of Geosciences, The University of Texas at Austin, 2305 Speedway Stop C1160, Austin, TX 78712, USA

Correspondence: Megan A. Mueller (megan.mueller@jsg.utexas.edu)

Abstract. Sedimentary provenance is a powerful tool for reconstructing convergent margin evolution. However, single mineral approaches, like detrital zircon, have struggled to track sediment input from mafic and metamorphic sources. Detrital rutile complements detrital zircon datasets by offering a path forward in sedimentary provenance reconstructions where metamorphic terranes are potential source regions. However, U–Pb geochronology in rutile can be difficult due to low uranium concentrations and incorporation of common Pb, and multiple workflows are currently in use. Here, we investigate U–Pb and trace element data reduction, processing, and common Pb correction workflows using new detrital rutile U–Pb geochronology and trace element geochemistry results from the Late Cretaceous to Eocene Central Sakarya and Sarıcakaya basins in Anatolia. A significant number of analyses were rejected (54 %) due to signal intensity limitations, namely low U, low Pb, anomalous signal, and inclusions. We identify this as a universal limitation of large-n detrital rutile studies and recommend the systematic reporting of the amount of discarded analysis and the processes for rejection in all studies using detrital rutile U–Pb geochronology. Additionally, we show that (1) the ^{208}Pb and ^{207}Pb common Pb reduction schemes produce similar age distributions and can be used interchangeably, while (2) the Stacey–Kramers distance is a suitable metric for quantifying U–Pb discordance, but a discordance filter is not recommended. (3) Instead, filtering U–Pb data by a power law function based on the corrected date uncertainty is appropriate. (4) The exclusion of low uranium concentration rutile biases date distributions and favors pelitic-derived, higher Zr-in-rutile temperature, and higher U–Pb concordance grains. (5) Paired U–Pb and trace elements can be used to evaluate potential bias in U–Pb data rejection, which reveals that data rejection does not bias the provenance interpretations. Finally, (6) The signature of sediment recycling can be identified through U–Pb dates and Zr-in-rutile temperatures. To better navigate the complexity of detrital rutile datasets and to facilitate the standardization of data reporting approaches, we provide open-access code as Jupyter notebooks for data processing and analysis steps, including common Pb corrections, uncertainty filters, discordance calculations, and trace element analysis.

1 Introduction

Sedimentary provenance analysis is widely used to reconstruct ancient sediment dispersal networks, source-to-sink sediment budgets, and sedimentary basin evolution and to discern links between tectonics, geodynamics, paleogeography, climate, and biologic evolution (Dickinson and Suczek, 1979; Garzanti et al., 2007; Clift et al., 2008; Gehrels, 2014; Blum and Pecha, 2014). Compositional provenance methods include sediment petrologic, chemical, and heavy mineral characterizations (e.g., Gazzi, 1965; Hubert, 1971; Dickinson and Suczek, 1979; Morton, 1985; Garzanti and Andò, 2007). Over the last several decades, the rise of chronometric and geochemical techniques led to the increase in single-mineral approaches. Detrital zircon U–Pb geochronology has become the most widely used technique as zircon is refractory and is abundant in crustal rocks (e.g., Gehrels, 2014). Further, the age, thermal history, and elemental and isotopic composition of detrital zircons can quantitatively reconstruct both sedimentary provenance and geodynamic, tectonic, and magmatic processes (Carrapa, 2010; Paterson and Ducea, 2015; Tang et al., 2020; Sundell et al., 2022). However, one major limitation is that zircons predominantly form in intermediate to felsic magmas, thus detrital zircon suites generally lack information about mafic igneous and metamorphic processes and sources (Hietpas et al., 2011; Moecher et al., 2011; Gaschnig, 2019). Zircon is present in metamorphic rocks as inclusions in other minerals or as recrystallized–dissolved–reprecipitated rims on zircon cores (Kohn and Kelly, 2017). The outer growth domains of zircons can be targeted with laser ablation–inductively coupled plasma–mass spectrometry (LA-ICP-MS) depth profiling or with spot analysis if the rims are thick enough, yet the most commonly used techniques for rapid provenance data acquisition do not routinely analyze zircon rims. Therefore, sedimentary provenance interpretations based on detrital zircon alone are incomplete. For this reason the sedimentary provenance community is increasingly turning to U–Th–Pb and trace elements in phases commonly used in petrochronology, such as detrital rutile (Zack et al., 2004a; Meinhold, 2010; Triebold et al., 2012; Bracciali et al., 2013; Rösel et al., 2014, 2019; O'Sullivan et al., 2016; Odlum et al., 2019; Pereira et al., 2020), detrital apatite (Morton and Yaxley, 2007; Chew et al., 2011; Mark et al., 2016; O'Sullivan et al., 2016, 2020), detrital monazite (Hietpas et al., 2010; Moecher et al., 2011; Gaschnig, 2019), and detrital titanite (Guo et al., 2020; Chew et al., 2020), in addition to other isotopic systems in these and other detrital minerals.

Detrital rutile is a complementary sedimentary provenance proxy to detrital zircon. Rutile forms in metamafic and metapelitic rocks across a range of pressure–temperature (P-T) conditions; therefore, detrital rutile is especially advantageous when tracking sediment input from greenschist to eclogite or granulite facies sources (e.g., Meinhold, 2010; Zack and Kooijman, 2017). The geochemical composition of rutile can further distinguish between metamorphic protoliths (e.g., Triebold et al., 2007, 2012; Meinhold, 2010). However, rutile U–Pb analysis is challenging due to low-U and low-radiogenic-Pb concentrations and due to the incorporation of initial non-radiogenic Pb. Here, we use a new detrital rutile petrochronology dataset from Anatolia to investigate data reduction, processing, and analytical steps in order to support robust provenance interpretations. In a number of studies, analyses have been discarded during U–Pb data reduction due to unacceptable signal intensity (e.g., Bracciali et al., 2013; Rösel et al., 2014, 2019), and we find that discarding analyses is a limitation to large-n detrital rutile datasets in the literature and this study. We test the sensitivity of resulting U–Pb date spectra to Pb correction methods, uncertainty and discordance filters, and a low U cutoff threshold. Ultimately, the new dataset demonstrates that detrital rutile captures sediment input from a subduction accretion complex that is poorly resolved in the detrital zircon record. Despite the described limitations, detrital rutile petrochronology can be effectively used to reconstruct sedimentary provenance, deformation, metamorphism, and sediment recycling.

2 Detrital rutile provenance

2.1 Detrital rutile synopsis

The advantages of detrital rutile provenance are extensively documented (e.g., Zack et al., 2004a; Meinhold, 2010; Triebold et al., 2012; Bracciali, 2019; Gaschnig, 2019; Pereira et al., 2020; Pereira and Storey, 2023), so we provide only a brief overview here. Rutile is the most common TiO_2 polymorph, a common accessory mineral in metamorphic and igneous rocks (Meinhold, 2010; Zack and Kooijman, 2017), and an abundant heavy mineral in sedimentary rocks (Morton, 1985). Rutile is present across a range of P-T conditions: rutile is generally stable at the surface and medium- to high-grade metamorphic conditions. Rutile can readily crystallize from titanite, ilmenite, and biotite during prograde metamorphism (Luvizotto et al., 2009; Meinhold, 2010; Cave et al., 2015). The breakdown of rutile to titanite occurs in prograde and retrograde environments, particularly in sub-greenschist to lower greenschist facies where titanite stability is favored (Cave et al., 2015; Zack et al., 2004b). Experimentally, rutile is stable above around 1.2–1.4 GPa in metagranitoids and hydrated basalts depending on compositional and chemical variability and in some cases can be stable down to 0.7 GPa (Xiong et al., 2005; Angiboust and Harlov, 2017). In subduction zone settings, rutile is especially abundant in eclogites (Klemme et al., 2002).

The chemical composition of rutile preserves original petrogenetic information. Rutile concentrates high field strength elements (Zr, Nb, Mo, Sn, Sb, Hf, Ta, W) through substitution with Ti that are commonly used as fingerprints of subduction zone metamorphism and crustal evolution (Foley et al., 2000; Rudnick et al., 2000). Detrital rutile geo-

chemistry fingerprints the lithologies of sediment sources in several unique ways: rutile concentrates the vast majority of available Nb, whereas Cr is non-selective and is distributed across metamorphic minerals; therefore, the Cr and Nb concentrations in rutile can discriminate between metamafic and metapelitic lithologies (Zack et al., 2004a, b; Triebold et al., 2011, 2012). Cr and Nb concentrations are attributed to different protoliths: generally metapelitic rutile (i.e., mica schists, paragneisses, felsic granulites) have less Cr than Nb contents, while metabasic rutile (i.e., mafic eclogites and granulites) have greater Cr than Nb contents (Zack et al., 2004b). Additionally, the incorporation of Zr in rutile is largely temperature dependent (Zack et al., 2004b; Watson et al., 2006; Tomkins et al., 2007; Ferry and Watson, 2007). Zirconium mobilizes during prograde metamorphic fluid release; the incorporation of Zr into rutile is buffered by coexisting quartz and zircon (Zack et al., 2004b). Zr contents in rutile correlate with peak metamorphic temperature and pressure conditions (Zack et al., 2004b; Watson et al., 2006; Tomkins et al., 2007; Kohn, 2020). Therefore, the Zr elemental composition in rutile is a commonly used thermometer, empirically and experimentally calibrated across a range of pressures and thermodynamic activity parameters (Zack et al., 2004b; Watson et al., 2006; Tomkins et al., 2007; Kohn, 2020). Zircon, quartz and rutile must be in equilibrium to use the Zr-in-rutile thermometer (e.g., Zack et al., 2004b), an assumption that likely holds in pelitic rocks (Pereira et al., 2021) but may not in mafic lithologies; however, this assumption is hard to evaluate in a detrital context. Inclusions in rutile can be used to determine whether rutile grew in equilibrium (Hart et al., 2016, 2018; see also Pereira and Storey, 2023, and references therein). In detrital rutile, removed from the petrologic system in which they formed and thereby missing key thermobarometric mineral associations, the Zr-in-rutile thermometer provides an estimate of the minimum peak metamorphic temperatures because the exact activity of SiO_2 in the original system is unconstrained (Kooijman et al., 2012; Triebold et al., 2012; Pereira et al., 2021; see also Meinhold et al., 2008; Rösel et al., 2019; Şengün et al., 2020; Zoleikhaei et al., 2021). For rutile of unknown source lithology, the calculated temperature is affected by the chosen pressure estimate. Pereira and Storey (2023) demonstrate this pressure dependence in detrital grains and recommend using the experimental and empirical calibration of Kohn, (2020; their Eq. 13) at an average pressure of 13 kbar with an uncertainty of 5 kbar:

$$T \ (°C) = \frac{71360 + 0.378 \times P - 0.130 \times C}{130.66 - R \times \ln} [C] - 273.15,$$

(1)

where P is the pressure in bars, C is the concentration of Zr in ppm, and R is the gas constant (8.3144 in $J\,mol^{-1}\,K^{-1}$).

Uranium is easily substituted for Ti^{4+} in rutile, making rutile a suitable mineral for U–Pb analysis. Rutile U–Pb analyses were first performed using thermal ionization mass spectrometry (TIMS) (Schärer et al., 1986; Mezger et al., 1989; Möller et al., 2000; Schmitz and Bowring, 2003; Kylander-Clark et al., 2008) and have since been collected with SHRIMP (Clark et al., 2000; Meinhold et al., 2010; Ewing et al., 2015), LA-MC-ICP-MS (Vry and Baker, 2006; Bracciali et al., 2013; Apen et al., 2020), LA-Q-ICP-MS (Storey et al., 2007; Zack et al., 2011), and LA-SC-ICP-MS (Kooijman et al., 2010; Okay et al., 2011; Smye and Stockli, 2014). As a high-temperature thermochronometer, U–Pb dates in rutile likely reflect mineral cooling through the closure temperature for volume diffusion of Pb (Dodson, 1973), which is between 400–640 °C in rutile. The temperature sensitivity of this partial retention zone in rutile is dependent on diffusion kinetics, cooling rate, chemistry, and grain size (Mezger et al., 1989; Cherniak, 2000). Rutile U–Pb dates may correspond to monotonic cooling from post-magmatic temperatures or cooling from the most recent medium to high-temperature metamorphic event that exceeded the closure temperature (Zack et al., 2004b; Zack and Kooijman, 2017). Slow cooling rates can produce rutile U–Pb dates significantly younger than the timing of peak metamorphism (e.g., Möller et al., 2000; Flowers et al., 2005). Because rutile U–Pb dates record thermal history information from conditions characteristic of the middle to lower crust (> 400 °C), U–Pb dates are ideal for inferring the timing and rate of deep-seated orogenic processes (Mezger et al., 1989; Möller et al., 2000; Flowers et al., 2005; Kylander-Clark et al., 2008; Smye et al., 2018) and of craton formation, stabilization, and cooling (Davis et al., 2003; Schmitz and Bowring, 2003; Blackburn et al., 2012). Furthermore, detrital rutile U–Pb geochronology is regularly used in sedimentary provenance analysis to reconstruct sedimentary basin evolution; paleoclimate and paleoenvironments; and orogen-scale deformation, exhumation, and sediment transport (Rösel et al., 2014, 2019; Mark et al., 2016; O'Sullivan et al., 2016; Pereira et al., 2020; Caracciolo et al., 2021; Clift et al., 2022).

2.2 Detrital rutile U–Pb challenge no. 1: low uranium content

Detrital rutile U–Pb petrochronology presents unique analytical, data reduction, and interpretation challenges. Uranium concentration in rutile varies among metamorphic protoliths: for example, rutile from mafic eclogites tend to have, on average, 75 % less U than those from metapelites (i.e., 5 vs. 21 ppm; Meinhold, 2010). The low U concentrations – from old rutile or sourced from mafic lithologies (cf. Sect. 6.2) – can make rutile challenging to date. To optimize data collection, some detrital rutile methods first analyze trace elements then only collect U–Pb data on rutile above a given U concentration threshold (ca. > 4–5 ppm; e.g., Zack et al., 2004a, 2011; Okay et al., 2011; Rösel et al., 2019). There is not a systematic relationship between uranium concentration and common Pb concentration. How-

ever, screening low-U rutile reduces the overall length of U–Pb analytical sessions and produces a higher proportion of concordant analyses (Zack et al., 2004a, 2011; Okay et al., 2011; Rösel et al., 2019). This protocol, however, introduces bias into the provenance results against metamafic rocks (cf. Sect. 6.2) and is generally discouraged (Bracciali et al., 2013; Bracciali, 2019). While this low-U screening is not necessarily common globally, it is a regional concern. There are four published detrital rutile U–Pb datasets from Türkiye, and two of the four (Okay et al., 2011; Şengün et al., 2020) only analyze U–Pb on detrital rutile with uranium concentrations above ca. 4–5 ppm. The two studies that do not use a U-threshold filter but instead analyze all detrital rutile grains (Shaanan et al., 2020; this study) must discard data due to very low uranium signals (below limit of detection). This includes discarding rutile grains that have low incorporation of U during growth (independent of analytical instrumentation) and rutile grains that have poorly resolved U–Pb ratios due to low-U CPS (counts per second) such as old rutile and mafic rutile (machine dependent). Omitting low-U rutile may make sense in some settings; however, this analytical approach likely biases provenance results as the concentration of uranium in rutile systematically varies by metamorphic protoliths, with mafic eclogites having lower U contents than metapelites (e.g., Meinhold, 2010). This potential bias is important to investigate as metamafic units in suture zones, presumably with low-U rutile, are expected to be a major contributor of detritus to many orogenic basins, including the northwestern Anatolian basins of this study.

2.3　Detrital rutile U–Pb challenge no. 2: common Pb incorporation

2.3.1　Common Pb correction overview

A second challenge with detrital rutile lies with data reduction and presentation. Because many detrital geochronologists are familiar with the zircon system, here we emphasize the differences in how U–Pb data should be treated in common Pb-bearing minerals vs. zircon. The U–Pb system in rutile is different from that of zircon due to the incorporation of common Pb, thereby requiring careful methodological choices on how to treat non-radiogenic Pb and U–Pb discordance. The zircon U–Pb system is "simple" in the sense that zircon incorporates negligible non-radiogenic initial Pb (i.e., common Pb) during crystallization, and Pb diffuses only at extremely high temperatures and in zircon with radiation damage (e.g., Schoene, 2014, and references therein). Thus, the majority of detrital zircon U–Pb analyses tend to be close to concordia, which makes data reduction and interpretation fairly straightforward, as even the ^{207}Pb/^{206}Pb dates of moderately discordant zircon are likely to be meaningful. Unlike zircon where discordant data exceeding a specified threshold are often discarded, it is not surprising that many rutile analyses may be discordant as rutile can incorporate a sig-

nificant amount of common Pb. In situ studies mitigate this by (1) regressing discordia lines through co-genetic analyses in Tera–Wasserburg space, where the lower intercept of the discordia with the concordia defines the U–Pb age of Pb diffusion closure (e.g., Faure, 1986; Chew et al., 2011; Vermeesch, 2020), or (2) applying a non-radiogenic Pb correction either by using an ad hoc Pb evolution model such as that of Stacey and Kramers (1975) or by measuring the composition of non-radiogenic Pb in a co-existing phase (e.g., Zack et al., 2004b). However, by nature, co-genetic grains in detrital samples are unknown, and a model therefore has to be applied. Below we review the common Pb correction calculations and discordance metrics for common Pb-bearing detrital minerals.

2.3.2　^{204}Pb correction

The basis of all common Pb correction approaches – ^{204}Pb, ^{207}Pb, and ^{208}Pb corrections – is to use a Pb evolution model (e.g., Stacey and Kramers, 1975) to find the fraction of total ^{206}Pb that is common ^{206}Pb and, by corollary, find the radiogenic ^{206}Pb fraction and then calculate the corrected date (Compston et al., 1984; Williams, 1997). We did not measure ^{204}Pb in this study and refer readers to other publications for ^{204}Pb correction details (Williams, 1997; Andersen, 2002; Storey et al., 2006; Chew et al., 2014). The ^{204}Pb correction method is valuable because it uses the non-radiogenic ^{204}Pb isotope and does not assume concordance, yet accurate measurement of ^{204}Pb is needed (in contrast, see Andersen, 2002), which can be challenging as ^{204}Pb is the least abundant Pb isotope. While accurate determination of the low-intensity ^{204}Pb peak is not a problem for TIMS or MC-ICP-MS instruments (e.g., Simonetti et al., 2005; Gehrels et al., 2008), it can require prohibitively long dwell times in single-collector instruments. Furthermore, the measurement of ^{204}Pb is complicated by the isobaric interference of ^{204}Hg introduced in the gas supply. In some cases, the concentration of ^{204}Hg can be reduced with traps or filters and back stripped by measuring ^{201}Hg or ^{202}Hg (e.g., Storey et al., 2006).

2.3.3　^{208}Pb correction

The ^{208}Pb correction method determines the common Pb component using the ^{232}Th-^{208}Pb decay scheme and assumes U–Th–Pb concordance, undisturbed Th/U, and no Pb loss. Because Pb loss is not considered, all corrected dates are (possibly) minimum ages. The ^{208}Pb correction is ideal for low-Th phases (Zack et al., 2011) and is commonly used for rutile, although not all rutile grains have low Th concentrations, and Th contents are often not reported. The equations here have been previously described in Williams (1997), Chew et al. (2011), and McLean et al. (2011) and as the total–Pb/U–Th scheme in Vermeesch (2020).

The proportion of $^{206}\text{Pb}_{\text{common}}$, f_{206}, is calculated as

$$f_{206} = \frac{\left(^{208}\text{Pb}/^{206}\text{Pb}_{\text{measured}}\right) - \left(^{208}\text{Pb}^*/^{206}\text{Pb}^*\right)}{\left(^{208}\text{Pb}/^{206}\text{Pb}_{\text{common}}\right) - \left(^{208}\text{Pb}^*/^{206}\text{Pb}^*\right)}, \quad (2)$$

where $^{208}\text{Pb}/^{206}\text{Pb}_{\text{measured}}$ is calculated directly from the raw data. The $^{208}\text{Pb}/^{206}\text{Pb}_{\text{common}}$ ratio is calculated from the two-stage Pb evolution model of Stacey and Kramers (1975) for dates older than 3.7 Ga as

$$\left(\frac{^{206}\text{Pb}}{^{204}\text{Pb}}\right)_{\text{common}} = 7.19 \cdot \left(e^{\lambda_{238} \cdot 4.57 \times 10^9} - e^{\lambda_{238} \cdot t_i}\right) + 9.307, \quad (3)$$

and

$$\left(\frac{^{208}\text{Pb}}{^{204}\text{Pb}}\right)_{\text{common}} = 33.21 \cdot \left(e^{\lambda_{232} \cdot 4.57 \times 10^9} - e^{\lambda_{232} \cdot t_i}\right) + 29.487, \quad (4)$$

or for dates younger than 3.7 Ga as

$$\left(\frac{^{206}\text{Pb}}{^{204}\text{Pb}}\right)_{\text{common}} = 9.74 \cdot \left(e^{\lambda_{238} \cdot 3.7 \times 10^9} - e^{\lambda_{238} \cdot t_i}\right) + 11.152, \quad (5)$$

and

$$\left(\frac{^{208}\text{Pb}}{^{204}\text{Pb}}\right)_{\text{common}} = 36.84 \cdot \left(e^{\lambda_{232} \cdot 3.7 \times 10^9} - e^{\lambda_{232} \cdot t_i}\right) + 31.23, \quad (6)$$

where using t_i is the uncorrected date in years ($^{206}\text{Pb}/^{238}\text{U}$ date from the iolite data reduction), the ^{232}Th decay rate λ_{232} is 4.9475×10^{-11} yr^{-1}, and the ^{238}U decay rate λ_{238} is 1.55125×10^{-10} yr^{-1} (Faure, 1986). The expected radiogenic $^{208}\text{Pb}^*/^{206}\text{Pb}^*$ ratios are calculated as

$$\frac{^{208}\text{Pb}^*}{^{206}\text{Pb}^*} = \left(\frac{^{232}\text{Th}}{^{238}\text{U}}\right) \cdot \left(\frac{e^{\lambda_{232} t_i} - 1}{e^{\lambda_{238} t_i} - 1}\right). \quad (7)$$

Following this, the radiogenic component, the $^{206}\text{Pb}^*/^{238}\text{U}$ ratio, can be calculated as

$$^{206}\text{Pb}^*/^{238}\text{U} = (1 - f_{206}) \cdot \left(^{206}\text{Pb}/^{238}\text{U}_{\text{measured}}\right). \quad (8)$$

Finally, the ^{208}Pb-corrected date ($^{206}\text{Pb}^*/^{238}\text{U}$ date) is calculated by solving the age equation with the $^{206}\text{Pb}^*/^{238}\text{U}$ ratio:

$$t_{206} = \frac{1}{\lambda_{238}} \cdot \ln\left(\frac{^{206}\text{Pb}^*}{^{238}\text{U}} + 1\right), \quad (9)$$

where t_{206} is the corrected date in years. The final corrected date is calculated iteratively, whereby each iteration replaces t_i with the previously calculated $^{206}\text{Pb}^*/^{238}\text{U}$ date. To test the sensitivity of the initial date estimate, we varied the initial date estimate, and therefore the initial common Pb composition, from 1 to 1000 Ma and, by the fifth iteration, the resulting ^{208}Pb-corrected date differs by less than 0.05 % for 98 % of the unknowns. The final ^{208}Pb-corrected date presented here is from the 200th iteration. The uncertainty of the date is calculated as the equivalent of the percent (propagated) uncertainty of the uncorrected $^{206}\text{Pb}/^{238}\text{U}$ ratio (Odlum et al., 2019).

2.3.4 ^{207}Pb correction

The ^{207}Pb correction method is based on a linear regression of $^{207}\text{Pb}/^{206}\text{Pb}$ and $^{238}\text{U}/^{206}\text{Pb}$ in Tera–Wasserburg space (Tera and Wasserburg, 1972) along a two-component mixing line between non-radiogenic and radiogenic Pb (Faure, 1986; Fig. S7). This method is most powerful for co-genetic minerals because it does not require knowing $^{207}\text{Pb}/^{206}\text{Pb}_{\text{common}}$. However, because co-genetic analyses are inherently unknown in detrital samples, the routine used here calculates the common Pb component of each individual analysis using the Stacey and Kramers (1975) two-stage Pb evolution model and an initial age estimate. The ^{207}Pb correction method assumes U–Pb concordance and no Pb loss but, unlike the ^{208}Pb correction, does not assume an undisturbed U/Th ratio. Because Pb loss is not considered, all corrected dates are (possibly) minimum ages. The equations given here are modified for detrital samples with unknown co-genetic minerals, previously described in Faure (1986), Williams (1997), Chew et al. (2011), and the semi-total-Pb/U scheme of Ludwig (1998) and Vermeesch (2020).

The calculation is similar to the ^{208}Pb correction. First, the proportion of $^{206}\text{Pb}_{\text{common}}$ is calculated as

$$f_{206} = \frac{\left(^{207}\text{Pb}/^{206}\text{Pb}_{\text{measured}}\right) - \left(^{207}\text{Pb}^*/^{206}\text{Pb}^*\right)}{\left(^{207}\text{Pb}/^{206}\text{Pb}_{\text{common}}\right) - \left(^{207}\text{Pb}^*/^{206}\text{Pb}^*\right)}, \quad (10)$$

where $^{207}\text{Pb}/^{206}\text{Pb}_{\text{measured}}$ is taken directly from the raw or reduced data. The $^{207}\text{Pb}/^{206}\text{Pb}_{\text{common}}$ ratio is based on the two-stage Pb evolution model of Stacey and Kramers (1975), which is calculated as the ratio of Eqs. (11) to (3) for dates older than 3.7 Ga or as the ratio of Eqs. (12) to (5) for dates younger than 3.7 Ga:

$$\left(\frac{^{207}\text{Pb}}{^{204}\text{Pb}}\right)_{\text{common}} = \frac{7.19}{137.88} \cdot \left(e^{\lambda_{235} \cdot 4.57 \times 10^9} - e^{\lambda_{235} \cdot t_i}\right) + 10.294, \quad (11)$$

or

$$\left(\frac{^{207}\text{Pb}}{^{204}\text{Pb}}\right)_{\text{common}} = \frac{9.74}{137.88} \cdot \left(e^{\lambda_{235} \cdot 3.7 \times 10^9} - e^{\lambda_{235} \cdot t_i}\right) + 12.998, \quad (12)$$

where t_i is the initial date estimate in years and the ^{235}U decay rate λ_{235} is 9.8485×10^{-10} yr^{-1} (Faure, 1986). Here, for t_i we use the $^{206}\text{Pb}/^{238}\text{U}$ date from the iolite data reduction. However, Chew et al. (2011) demonstrated that the choice of initial date results in a < 0.05 % difference in the final ^{207}Pb-corrected date after five iterations. The expected radiogenic $^{207}\text{Pb}/^{206}\text{Pb}^*$ ratio is calculated as

$$\frac{^{207}\text{Pb}^*}{^{206}\text{Pb}^*} = \left(\frac{^{235}\text{U}}{^{238}\text{U}}\right) \cdot \left(\frac{e^{\lambda_{235} t_i} - 1}{e^{\lambda_{238} t_i} - 1}\right), \quad (13)$$

where $^{235}\text{U}/^{238}\text{U}$ is 137.88 (Steiger and Jäger, 1977). Finally, the radiogenic component, the $^{206}\text{Pb}^*/^{238}\text{U}$ ratio, can be calculated using Eq. (8) and then used to solve the age equation (Eq. 9). As with the ^{208}Pb correction, to iteratively

calculate the date, each iteration replaces t_i with the previously calculated $^{206}Pb^*/^{238}U$ date. The ^{207}Pb-corrected date presented here is from the 200th iteration. The uncertainty of the date is calculated as the equivalent of the percent (propagated) uncertainty of the uncorrected $^{206}Pb/^{238}U$ ratio (Odlum et al., 2019). For example, if the initial $^{206}Pb/^{238}U$ ratio has 2 % uncertainty at 2 sigma and the corrected date is 200 Ma, then the corrected date uncertainty is ±4 Ma (2s).

2.3.5 Discordance

Although there are various ways to calculate the discordance of U–Pb analyses, which are reviewed elsewhere (e.g., Vermeesch, 2021), it remains unclear which metric is best for common Pb-bearing minerals and if a discordance threshold should be applied. One family of discordance metrics relies on the difference between the $^{206}Pb/^{238}U$ date and $^{207}Pb/^{206}Pb$ date (e.g., Gehrels, 2011). Because ^{207}Pb and ^{208}Pb corrections force concordance, these metrics are not applicable to common Pb-bearing minerals. One metric potentially relevant to common Pb-bearing minerals is the Stacey–Kramers distance (after Vermeesch, 2021; see Sect. S3 in the dataset for further discussion). The Stacey–Kramers distance is calculated by first using the U–Pb analysis and $^{207}Pb/^{206}Pb_{common}$ composition (calculated during common Pb correction) to find the discordia in Tera–Wasserburg space, then discordance is calculated as the distance between the measured $^{238}U/^{206}Pb$ and $^{207}Pb/^{206}Pb$ coordinates and the concordia intersection (δ_2) along the total discordia line distance ($\delta_1 + \delta_2$) (Fig. S7; Vermeesch, 2021):

$$\text{Concordance} = \delta_1/(\delta_1 + \delta_2). \quad (14)$$

If a discordance threshold is applied, the Stacey–Kramers distance approach includes more young dates than old dates (> 1000 Ma) due to the change in concordia slope around 1000 Ma (Fig. S7; Vermeesch, 2021). The application of a discordance threshold has been underexplored in detrital rutile, with most studies applying no discordance filter, perhaps due to the lack of consensus on how to define discordance in common Pb-bearing minerals. Rather, a group of studies proposes to filter analyses based on the percent uncertainty of the corrected date (Mark et al., 2016; Govin et al., 2018; Chew et al., 2020; Caracciolo et al., 2021). It is noted that there is little guidance on how uncertainties are calculated and propagated during Pb correction, which ought to be investigated in future work; meanwhile, the filters should be applied with care. We explore these thresholds with our new dataset.

3 Geologic context

Anatolia is composed of a series of subduction complexes, island arcs, and continental terranes that accreted and collided from the Late Paleozoic through Cenozoic during the progressive opening and closing of Paleotethys and Neotethys seaways (Şengör and Yilmaz, 1981). Today, northwestern Anatolia comprises, from structurally highest (north) to lowest (south), the continental Pontides, including the Cretaceous–Eocene forearc-to-foreland Central Sakarya and Sarıcakaya basins, the Permian–Triassic Karakaya Complex, the İzmir–Ankara–Erzincan suture zone and associated Neotethys ophiolites and mélange, and the lower plate Anatolide–Tauride continental terranes (Fig. 1). The Pontides basement contains Paleozoic paragneiss, schist, and amphibolite rocks intruded by Carboniferous granitoids emplaced during the Variscan orogeny (Göncüoğlu et al., 2000; Ustaömer et al., 2012). The nature of the Karakaya Complex is debated but is generally considered a subduction–accretion complex associated with the Late Paleozoic–Early Mesozoic closure of the Paleotethys along the southern margin of Eurasia (Pickett and Robertson, 1996; Okay and Göncüoglu, 2004; Federici et al., 2010; Ustaömer et al., 2016). The Karakaya Complex contains metamafic and metasedimentary rocks interpreted as seamounts of intra-oceanic basaltic composition and forearc basin and trench deposits (Pickett and Robertson, 1996) that were subsequently metamorphosed to blueschist and epidote–amphibolite with minor eclogite facies with estimated temperatures of $340–550 \pm 50$ °C (Okay et al., 2002; Federici et al., 2010) with phengite, glaucophane, and barroisite Ar–Ar cooling dates around 200–215 Ma (Okay et al., 2002). The youngest Karakaya Complex units are unmetamorphosed or metamorphosed to zeolite to lower greenschist facies (120–376 °C) (Federici et al., 2010) and are unconformably overlain by Jurassic platform carbonates. The Cretaceous to present closure of the Neotethys and associated suturing is recorded in the Central Sakarya and Sarıcakaya basins located north of the suture zone. Stratigraphic and paleocurrent (Ocakoğlu et al., 2018), provenance (Mueller et al., 2022; Campbell et al., 2023), and mudstone geochemistry records (Açıkalın et al., 2016) show the input of suture-zone-derived material into the Central Sakarya Basin from the Late Cretaceous through Eocene, interpreted as progressive suture zone uplift and exhumation during continental collision (Ocakoğlu et al., 2018; Okay et al., 2020; Mueller et al., 2022; Campbell et al., 2023). Cretaceous subduction-related arc volcanism and Paleogene syn-collisional volcanic centers are located within and to the north of the basins (Kasapoğlu et al., 2016; Ersoy et al., 2017, 2023; Keskin and Tüysüz, 2018). By Eocene times, continued collision increased plate coupling that manifested as increased contractional deformation that activated the basement-involved Tuzaklı–Gümele Thrust (also termed the Söğüt Thrust or Nallıhan Thrust) and partitioned the southern Central Sakarya Basin into the Sarıcakaya Basin (Mueller et al., 2022). The Eocene Sarıcakaya Basin received sediment from the suture zone and Karakaya Complex to the south and basement-involved thrust sheets to the north (Mueller et al., 2019).
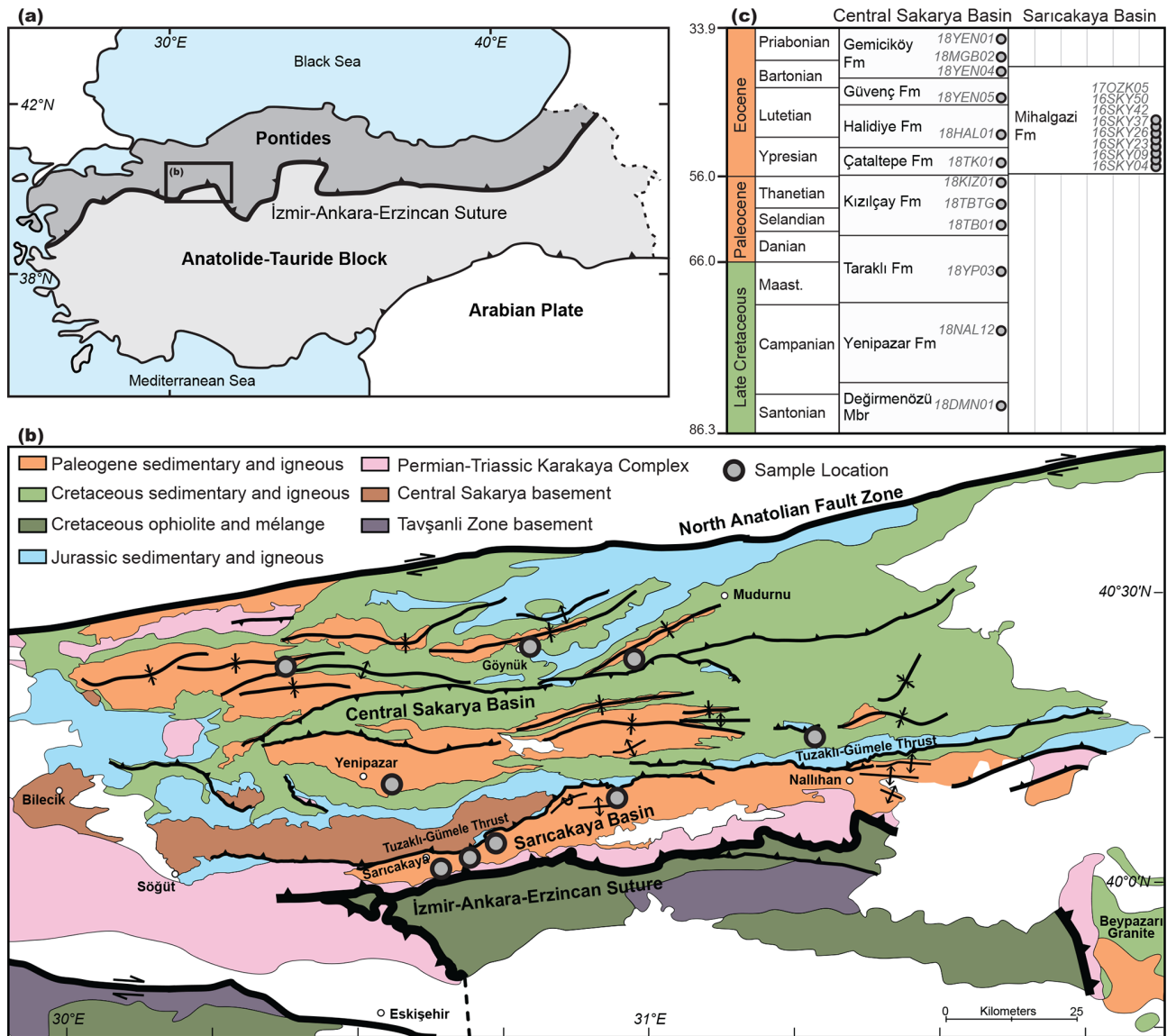
Figure 1. (a) Simplified terrane map of Anatolia and **(b)** geologic map of the Central Sakarya Basin and Sarıcakaya Basin region (after Aksay et al., 2002). **(c)** Simplified stratigraphic correlation chart and schematic sample distribution. Stratigraphy after Ocakoğlu et al. (2018).

4 Methods

4.1 Sample information

Sedimentary rock samples were collected from Upper Cretaceous to Eocene siliciclastic sections in the Central Sakarya Basin and Sarıcakaya Basin in western Anatolia (Fig. 1; Table S1). Detrital zircon U–Pb ages and Hf isotopes from these samples are already published (cf. Sect. 8; Mueller et al., 2019, 2022; Campbell et al., 2023); a set of 20 samples were chosen for detrital rutile U–Pb and trace element analyses. Heavy minerals were extracted using standard heavy mineral techniques, including crushing, water table, heavy liquid, and magnetic separation (see supplemental text in the data repository). Rutile grains were handpicked from the

≥ 0.3 amp. magnetic fraction using a Leica M205C binocular microscope. Three samples – 16SKY26, 16SKY42, and 17OZK05 – yielded hundreds of rutile grains, and we hand-picked 260–320 rutile grains from each sample, whereas all grains were picked from samples with smaller yield. The low yield of rutile grains partially contributes to the low-n date distributions of the individual samples. Rutile grains were mounted in epoxy and polished to expose the internal structure. Rutile mounts were carbon coated and imaged with a TFS Apreo-S with Lovac scanning electron microscope (SEM) with an energy-dispersive detector (EDS) to distinguish TiO_2 grains from other heavy minerals (Fig. S1).

4.2 U–Pb analytical protocol

Detrital rutile U–Pb geochronology was conducted at the Isotope Geochemistry Lab at the University of Kansas (KU-IGL) using a Thermo Element2 magnetic sector field ICP-MS coupled to a Photon Machines AnalyteG2 excimer laser ablation system. The protocol was modified from Rösel et al. (2019) to optimize for low U contents (Sect. S1; Table S2). The ICP-MS was manually tuned using NIST SRM 612 reference material glass to optimize for high sensitivity and low oxide production. Grains were ablated for 25 s with a laser beam diameter of 50 μm, laser fluence of 3.0 J cm^{-2}, and 10 Hz repetition rate. The U–Pb data were collected in four analytical sessions. The analytical protocol was modified from session to session to optimize for the analysis of low U and Pb unknowns and high U and Pb reference materials. In the first two analytical sessions, 21RtF and 21RtG, Pb and Th isotopes were measured with the secondary electron multiplier operating in counting detection mode, whereas Pb and Th isotopes were measured with the secondary electron multiplier in both counting and analog modes ("both mode") for the final two sessions, 21RtA and 21RtB. Primary and secondary reference materials were R10 (1091.6 ± 3.5 Ma by TIMS, 2 s abs.; Luvizotto et al., 2009), Wodgina (2845.8 ± 7.8 Ma by TIMS; Ewing, 2011), 9826J (381.9 ± 1.1 Ma by TIMS; Kylander-Clark, 2008), LJ04-08 (498 ± 3 Ma by LA-ICP-MS; Apen et al., 2020), and Kragerø (1085.7 ± 7.9 Ma by TIMS; Kellett et al., 2018). For U–Pb analyses, the analysis of five to eight unknowns was followed by two standards, the primary standard R10 and one of the secondary standards. The data were reduced in iolite 4 (Paton et al., 2011), calibrated against R10 uncorrected for initial Pb, and using the weighted linear fit drift correction which reproduced secondary standard ages and brought their mean square weighted deviation (MSWD) closest to 1. The concordia ages are satisfactory for all reference materials, except for the Wodgina and Kragerø, which did not perform well during the first two analytical sessions – likely due to ^{206}Pb counts per second exceeding the limit of linear behavior in counting detection mode – and are discarded from those analytical sessions. Standard reproducibility is discussed further in the supplemental text included in the data repository; U–Pb data are provided in the data repository (Mueller et al., 2023).

4.3 Trace element geochemistry analytical protocol

Detrital rutile trace element geochemistry (^{49}Ti, ^{51}V, ^{53}Cr, ^{66}Zn, ^{69}Ga, ^{90}Zr, ^{93}Nb, ^{95}Mo, ^{118}Sn, ^{121}Sb, ^{177}Hf, ^{181}Ta, ^{182}W) was conducted at the KU-IGL using the same instrumentation and parameters, except with a 25 or 35 μm spot size. Reference materials included USGS GSD-1G and USGS GSC-1G glasses (Jochum et al., 2011) and R10 rutile (Luvizotto et al., 2009). For trace element analysis, the analysis of 5–10 unknowns was followed by analysis of two standards, the primary standard GSD-1G and one of the sec-

ondary standards. Trace element concentrations were calculated using the "Trace Element" routine in iolite 4 with ^{49}Ti as an internal standard; for rutile unknowns, TiO$_2$ was set to be 100 mass-% (e.g., Plavsa et al., 2018; Rösel et al., 2019). Standard reproducibility is discussed in the supplemental text in the data repository (Sect. S2). In short, for the secondary standard GSC-1G, all elements are within 10 % of the published values except for Sn and Ga, and for the secondary standard R10, all results are within the range of reported values. Following U–Pb and trace element analysis, mounts were imaged in an SEM at University of Nevada Reno (Fig. 2). Most grains have both U–Pb and trace element results, but some grains have only U–Pb results due to the grains being too small for a second ablation spot or only trace element results due to discarded U–Pb data. Detrital rutile trace element data are given in the data repository (Mueller et al., 2023).

4.4 Additional data workflows

Additional data reduction and data calculations steps were performed. Provided as a complement to this paper are open-access Jupyter notebooks that contain the Python and R code used to perform these additional calculations and to generate figures, which are briefly described here (Mueller, 2024). (1) The ^{208}Pb and ^{207}Pb corrections were performed in the "Detrital-Common-Pb-Corrections" notebook using the equations detailed in Sect. 2 above. The notebook allows for either a manually set number of iterations or to iterate until all analyses are below a given threshold – the percent difference in corrected date between the current and previous iteration. Presented here are the results from the 200th iteration. (2) The UPb-Plotter notebook visualizes uncorrected U–Pb results in Tera–Wasserburg space, compares metrics for excluding analyses based on uncertainty filters (Sect. 5.3), and calculates discordance using the Stacey–Kramers and Aitchison distances (Sects. 2, S3; Figs. S7–S8). (3) The "Rutile-Trace-Elements" notebook includes the calculations and resulting figures for exploring TiO$_2$ polymorphs, mafic and pelitic protoliths, Zr-in-rutile thermometry, and low U contents. Discrimination diagrams using V, Cr, Zr, Fe, and Nb distinguish rutile from other TiO$_2$ polymorphs (Triebold et al., 2011), and all analyzed grains plot within the rutile field (Fig. S2). Rutile grains are classified as mafic or pelitic based on the Cr–Nb discrimination fields of Triebold et al. (2012), and Zr-in-rutile temperatures are calculated with the Kohn (2020) formulation (Eq. 1) at 13 kbar. (4) The "Detrital-PCA-R" notebook performs principal component analysis on trace element data using the pcaCoDa function in the robCompositions library, which is designed to handle compositional data (Templ et al., 2011). (5) Additionally, the "UPb-Timeseries" notebook is provided for visualizing U–Pb time series data.

5 U–Pb geochronology results

5.1 U–Pb data quality

A total of 1278 detrital rutile grains were analyzed for U–Pb geochronology. A significant number of analyses were rejected and excluded, as discussed below. We aim to be transparent in data reporting – including the number of grains analyzed and the criteria for rejection – in order to give precedence for this practice, which is missing in the literature, and to explore the current limitations of large-n detrital rutile studies. Even with the optimized LA-ICP-MS protocol, a significant number of analyses did not meet quality control goals: 665 of 1277 (54 %) analyses were rejected due to anomalous (spiky) patterns in raw signal intensity, or low U or low Pb signal intensity. Figure 2 depicts representative examples of signal intensity in accepted and rejected analyses. Inclusions and anomalous patterns were easily spotted through monitoring ^{206}Pb, ^{207}Pb, ^{238}U, ^{232}Th, ^{206}Pb/^{238}U, and ^{207}Pb/^{206}Pb channels. In some instances, the signal of an inclusion or anomalous (spiky) pattern was short enough that the integration window could be shortened to exclude it. In other cases, the non-inclusion signal could not be isolated and the entire analysis was discarded. Potential causes for the abnormal signal patterns and high Pb uncertainty include (1) elemental heterogeneity from ablating into small inclusions and/or lamellae, (2) inhomogeneities due to microcracks with different element or isotope composition, (3) heterogeneous amount of common lead incorporation during rutile growth, and (4) textural and/or elemental heterogeneities due to multiple rutile growth events. However, scenarios 3 and 4 are unlikely for Pb because it diffuses and should not cause spikes.

The SEM images do not give a clear picture of how to better select grains that will produce acceptable signal intensity and U–Pb concordance. Figure 2 shows SEM images of representative rutile grains after laser ablation. All grains appeared inclusion free before ablation, yet some analyses clearly ablated into inclusions (Fig. 2b, e). The large laser spot size of 50 μm gives a higher signal, which is better for grains with potentially low U or low Pb concentrations, but the potential trade-off is increasing the likelihood of hitting inclusions. Grains with obvious inclusion lamellae generally yielded poor data quality.

5.2 U–Pb geochronology and common Pb correction results

The uncorrected U–Pb results are displayed in Fig. 3. We note that all concordia diagram figures display the uncorrected U–Pb data; common Pb corrections force concordance and the corrected data are displayed as date distributions. A number of analyses plot close to the concordia curve and many plot along the discordia trend toward common Pb values. Both ^{208}Pb and ^{207}Pb corrections were performed on the uncorrected U–Pb analyses. After 200 iterations, the ^{208}Pb and ^{207}Pb corrections resulted in 547 and 487 corrected dates between 0 and 4500 Ma, respectively. These numbers differ because no corrected date is calculated when the proportion of ^{206}Pb$_{common}$ is greater than 1 and because the common Pb corrections can yield dates younger than 0 Ma or significantly older than 4500 Ma depending on the calculated proportion of ^{206}Pb$_{common}$ (f_{206}). The Pb-corrected U–Pb data are shown in Fig. 4 as kernel density estimates (KDEs) and cumulative distributions. The date distributions of individual samples are given in Fig. S9, but due to small sample sizes, interpretations are based on the cumulative dataset.

The two different Pb corrections produce similar date distributions (Fig. 4). For both distributions, the main date peak is at ca. 185 Ma, with a minor peak around 297 Ma. The ^{207}Pb and ^{208}Pb distributions vary in the presence and amplitude of minor Paleozoic and older populations. The ^{208}Pb correction results include more Devonian and older grains ($n = 131/547$, 24 %) than the ^{207}Pb correction ($n = 68/487$, 14 %).

5.3 Uncertainty and discordance thresholds

Detrital U–Pb data can be further filtered by U–Pb ratio uncertainty, date uncertainty, or discordance thresholds. Because the uncertainty on the corrected date is calculated from the uncertainty on the measured ^{206}Pb/^{238}U ratio (cf. Sect. 2), these metrics are similar. Figure 5 displays the results of three uncertainty threshold filters: (1) 20 % uncertainty on ^{238}U/^{206}Pb and ^{207}Pb/^{206}Pb ratios (modified from Lippert, 2014), (2) a date-dependent filter that excludes analyses with > 10 % date uncertainty for corrected dates > 100 Ma, > 20 % uncertainty for dates 10–100 Ma, or > 25 % uncertainty for dates < 10 Ma (after Govin et al., 2018), and (3) a power law threshold that excludes analyses if the percent uncertainty on the ^{207}Pb-corrected date exceeds the function: $(t^{-0.65}) \cdot 8$ (after Chew et al., 2020). The results of these filters are displayed as uncorrected U–Pb data in Tera–Wasserburg space and ^{207}Pb-corrected date distributions (Fig. 5). From the total ^{207}Pb-corrected analyses ($n = 487$), the above thresholds exclude an additional 108 (22 %), 191 (39 %), and 46 (9 %) analyses, respectively. The power law function excludes the fewest number of analyses.

The three filters have similar ^{207}Pb-corrected date distributions (Fig. 5). The main age modes identified in all three filters are 183, 300, and 400 Ma. Minor Devonian and older date modes are present. Only the date-dependent filter identifies the 88 Ma date mode, and it includes a 9 Ma mode that is significantly younger than the youngest sampled strata (Bartonian-Priabonian). The U–Pb ratio uncertainty and power law filters have nearly identical date peaks, with the power law filter including more grains, especially in the ~ 183 Ma mode.

The Stacey–Kramers distance is used to quantify discordance in common Pb-bearing minerals (Sect. S3; Fig. S7).
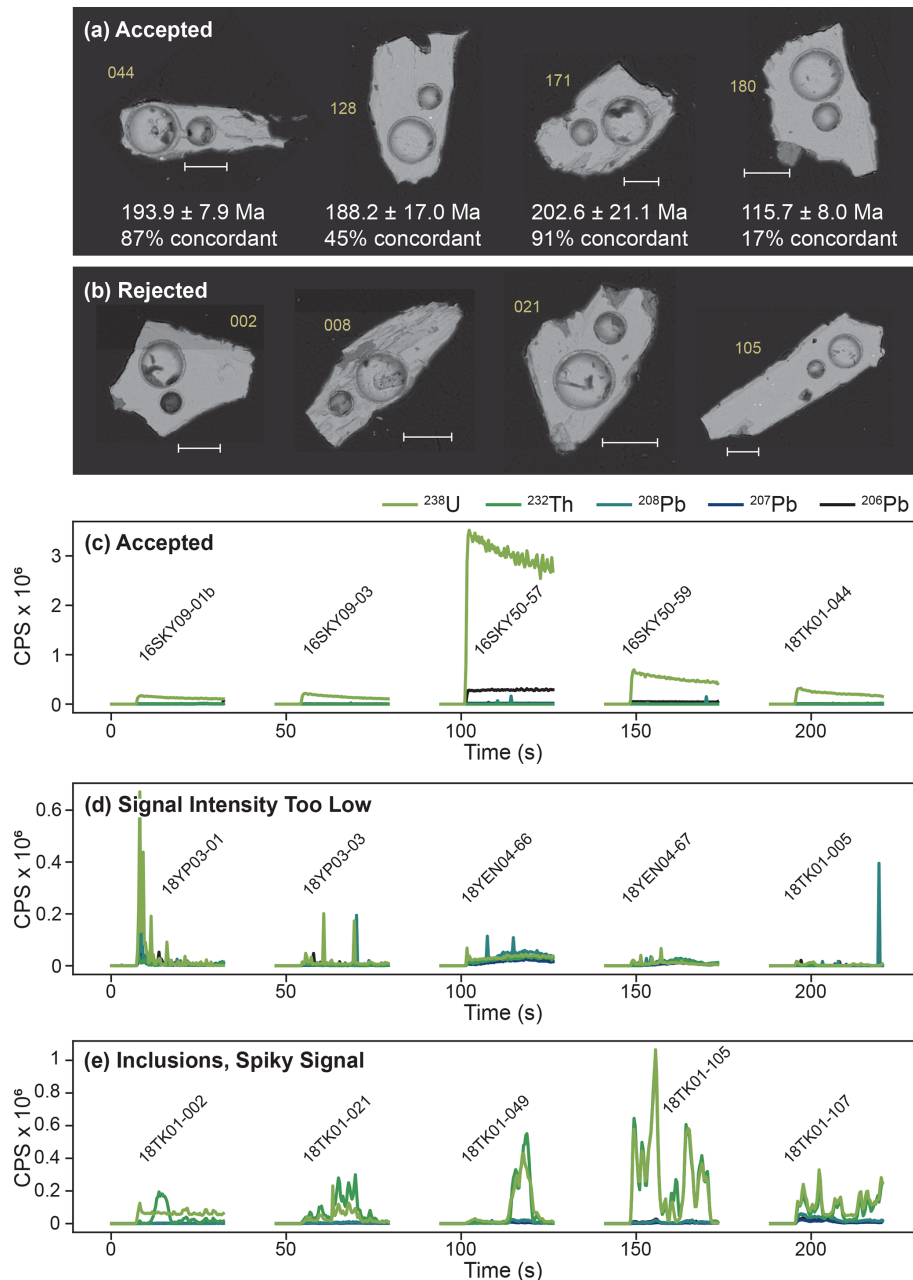
Figure 2. Scanning electron microscope backscattered electron (SEM BSE) images and U–Pb signal intensities of representative rutile grains. **(a)** Rutile grains with acceptable U–Pb analyses across a range of concordance. U–Pb date and concordance are from the [207]Pb correction method and Stacey–Kramers metric, respectively. Ablation pits are from U–Pb analysis (larger) and trace element analysis (smaller). The scale bar is 50 µm. All grains are from sample 18TK01; the grain number is in yellow. **(b)** Images of rutile grains with U–Pb analyses rejected because of inclusions (18TK01-002) or spiky signal (18TK01-008, -021, -105). **(c–e)** Representative U–Pb raw signal intensity patterns of accepted analyses **(c)** and rejected analyses from too low signal intensity **(d)** or inclusions and/or spiky signal **(e)**.

The results are shown in Fig. S8 in Tera–Wasserburg space with uncorrected U–Pb analyses colored by distance (concordance). In the Stacey–Kramers distance formulation, analyses closest to the common Pb composition are considered most discordant (Figs. S7 and S8). The Stacey–Kramers distance appears to reflect U–Pb systematics in common Pb-bearing minerals and is a representative metric of discordance. Figure 6 displays the [207]Pb-corrected date distributions filtered using the power law threshold and subdivided into bins based on their Stacey–Kramers concordance values. The 100 %–80 % concordance group has the most discrete date modes at 189, 307, 608, and 1593 Ma. The 80 %–
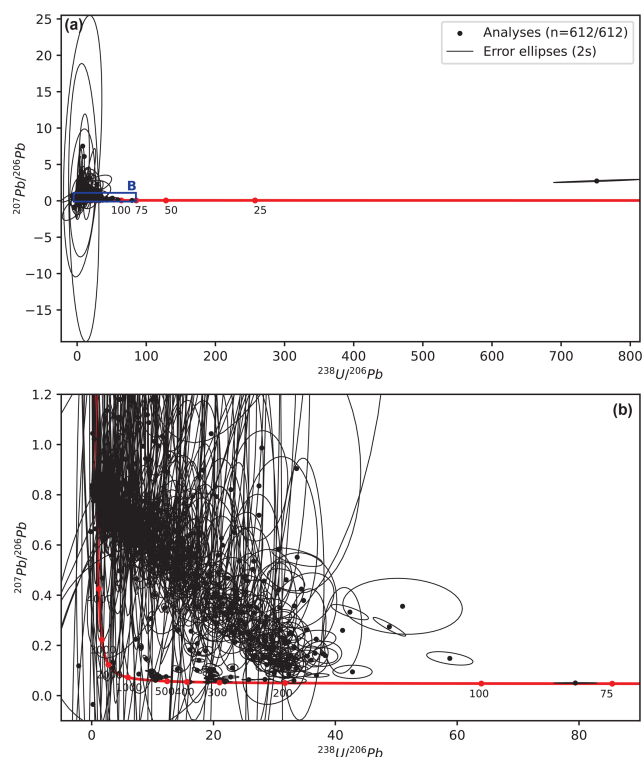
Figure 3. Uncorrected detrital rutile U–Pb results displayed in Tera–Wasserburg space. Uncertainty ellipses are 2 s propagated. The area displayed in **(b)** is highlighted by the blue box in **(a)**.

60 %, 60 %–40 %, and 40 %–0 % bins have unimodal age distributions that are asymmetric toward older dates and have a dominant age mode around 180 Ma. The cumulative distributions reveal that the distribution of all grains together has a similar distribution to that of the 40 %–0 % group (Fig. 6, top). Comparison of the distribution of all grains together to the 100 %–80 % concordance group reveals that if a 20 % discordance filter were applied similar to detrital zircon U–Pb workflows, the same general date modes would be identified. However, the addition of lower-concordance grains (i.e., 80 %–0 % concordance groups) broadens the Jurassic peak and shifts it slightly younger from 189 to ∼ 180 Ma, decreases the amplitude of the Carboniferous and Proterozoic peaks, and increases the amplitude of the ∼ 400–450 Ma peaks.

6 Trace element geochemistry results

6.1 Metamorphic protolith

The Cr and Nb concentrations discriminate between metapelitic and metamafic source rocks (Zack et al., 2004a; Triebold et al., 2011, 2012). Even though there are multiple proposed discrimination lines between metamafic and metapelitic source lithologies (e.g., Meinhold et al., 2008; Triebold et al., 2012), the detrital rutile in this dataset plot

in both the metamafic (33 %) and metapelitic (67 %) fields (Fig. 7a). There is no clustering of protolith by U–Pb date, with prominent date modes containing both metamafic and metapelitic grains (Fig. 7b). While some metamafic grains plot close to concordia (more concordant), many plot close to the common Pb composition concordia intercept (more discordant).

6.2 Zr-in-Rutile temperature and uranium concentration

The Zr-in-rutile temperatures were calculated using the Kohn (2020) calibration (Eq. 1) at 13 kbar with an uncertainty of 5 kbar; results are included in the data repository. The Zr concentrations range from 2 to 1934 ppm, yielding source rock minimum peak temperatures from 336 ± 15 to 849 ± 28 °C. The Zr-in-rutile temperature results are displayed alongside U concentration and colored by protolith (Fig. 8). There is not a correlation between Zr-in-rutile temperature and protolith. The majority of grains have moderate temperatures corresponding to greenschist to blueschist facies conditions: 68 % ($n = 147/216$) of mafic and 67 % ($n = 301/446$) of pelitic grains are below 500 °C. There are fairly consistent Zr-in-rutile temperatures within the dominant date modes – 90, 185, 300, 500–650 Ma (Fig. 9). The highest temperatures, reaching granulite facies conditions, are found in the 90 Ma date mode. The 500–650 and 300 Ma rutile grains similarly preserve high temperatures, up to 700–820 °C, whereas the majority of 185 Ma grains have temperatures in greenschist to blueschist facies around 450–550 °C.

The uranium concentrations range from 0.002 to 113 ppm. These low values are above the detection limit. The primary standard, R10, has a U concentration of 44 ppm (Luvizotto et al., 2009) and, in our measurements, on average, 2.1 million CPS ^{238}U (i.e., ∼ 50 000 counts/ppm). The ^{238}U baseline was about 5 CPS, therefore, the instrument setup has a detection limit of about 0.0003 ppm ^{238}U (calculated from 3× background). All analyses are above the detection limit, with 91 % ($n = 555/612$) of analyses at least an order of magnitude above this limit.

The comparison of Zr-in-rutile temperatures with U concentration reveals that the majority of low-U rutile samples (< 4 ppm) are within greenschist to blueschist facies conditions (68 %, $n = 205/303$ below 500 °C; Fig. 8). Additionally, mafic-classified grains are dominantly low U (95 %, $n = 106/112$ below 4 ppm). The majority of rutile with U contents above 4 ppm are classified as pelitic (85 %, $n = 34/40$) and generally have higher Zr contents.

7 Discussion

7.1 Recommendations for U–Pb data rejection, correction, and filtering

The complex, natural dataset presented here allows an examination of the current practices of data reporting and limita-
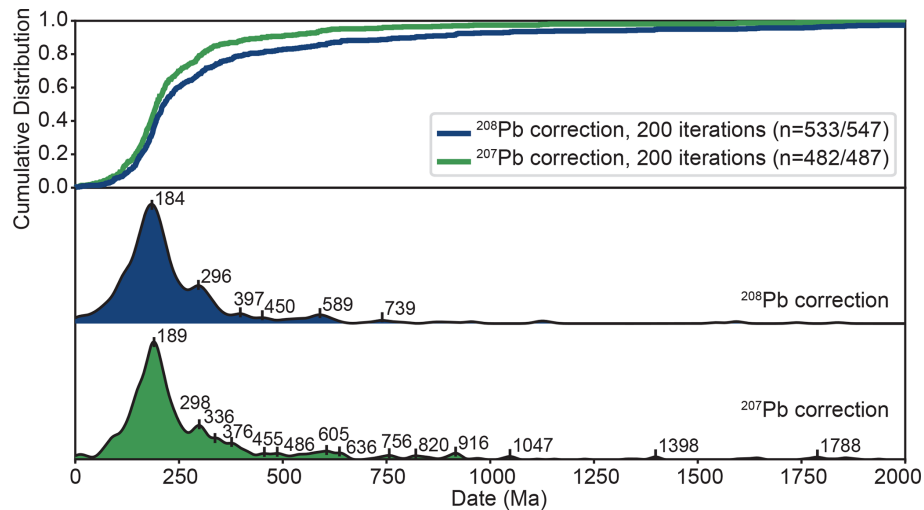
Figure 4. The ^{208}Pb- and ^{207}Pb-corrected date distributions from 0 to 2000 Ma displayed as normalized kernel density estimates and cumulative distributions, visualized with detritalPy (Sharman et al., 2018). No discordance or uncertainty filter is applied.
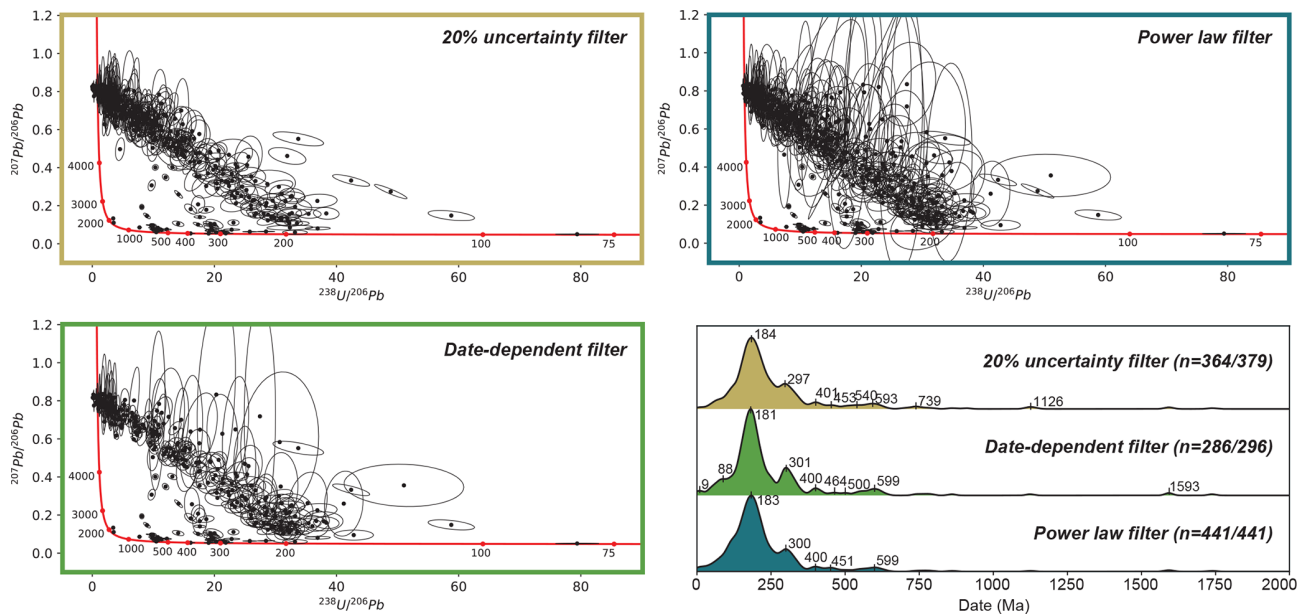

Figure 5. Comparison of U–Pb data filters based on U–Pb ratio and date uncertainties, displayed in Tera–Wasserburg space (uncorrected) and normalized kernel density estimates (^{207}Pb-corrected). The U–Pb ratio uncertainty filter (yellow) excludes all analyses with ^{238}U/^{206}Pb and ^{207}Pb/^{206}Pb ratio uncertainties above 20 % (modified from Lippert, 2014). The date-dependent filter (green) excludes analyses based on the ^{207}Pb-corrected date and uncertainty (see text; after Govin et al., 2018). The power law filter (blue) excludes analyses if the percent uncertainty on the ^{207}Pb-corrected date exceeds the given power law function (see text; after Chew et al., 2020).

tions of large-n detrital rutile studies. In this study, a large number of analyses were rejected during U–Pb data reduction, but the SEM images do not provide simple criteria (e.g., inclusions, fractures) for how to better select grains that will produce acceptable signal quality or lower U–Pb discordance (Fig. 2). All areas selected for analysis appeared inclusion free before ablation, yet some analyses evidently ablated into inclusions (Fig. 2b,e). Because we expected grains from

mafic sources with low U or low Pb concentrations, we used a large 50 µm laser beam diameter, but this potentially increased the probability of hitting inclusions. While rejecting analyses is not ideal, low U and Pb signal intensities are not unexpected in natural samples, so some degree of data rejection is to be anticipated, especially given the predicted metamafic (very low U) protolith sources. We contend here that the exclusion of data from interpretation is common to many
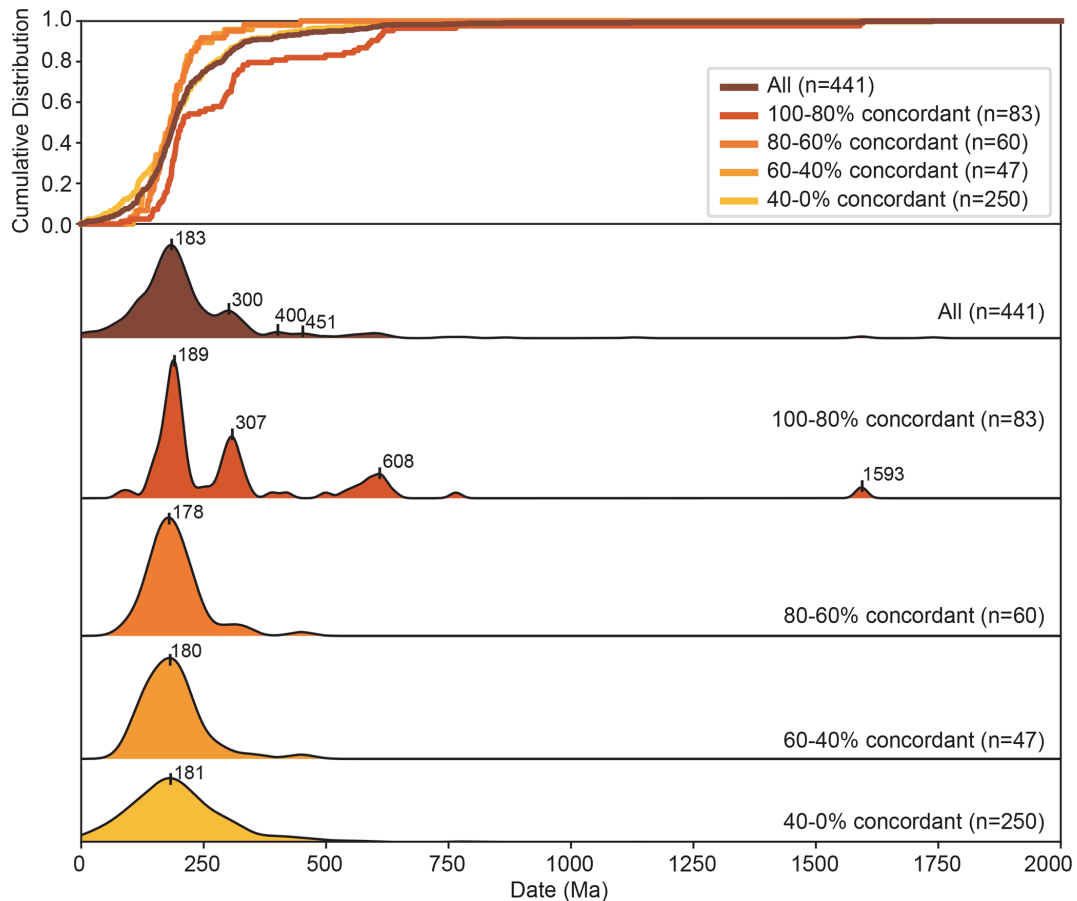
Figure 6. Relative kernel density estimates (KDEs; bottom panels) and cumulative distributions (top) of ^{207}Pb-corrected, power law uncertainty-filtered dates categorized by discordance from Stacey–Kramers distance values.

detrital rutile studies (e.g., Bracciali et al., 2013; Rösel et al., 2014, 2019; Caracciolo et al., 2021), ours included. However, in most studies, the number of discarded analyses and criteria for discarding analyses during U–Pb data reduction are unclear or not mentioned, thereby limiting opportunities to evaluate data quality and navigate results in a potentially meaningful way. We recommend that these criteria be explicitly stated and discussed in all studies using detrital rutile U–Pb geochronology.

We reiterate that the number of discarded analyses is surprising but is the result of a natural dataset and not an analytical or data reduction error. Daily instrument tuning on NIST 612 glass produced stable signal, high count rates, and low oxide production (Table S2); therefore, the grains rejected due to "spiky" raw signal intensity are not a sign of poor instrument setup. Further, a comparison of U–Pb precision between our results and other rutile U–Pb studies (Fig. S12; Jenkins et al., 2023; Bracciali et al., 2015; Odlum et al., 2024) demonstrates that, for rutile with U concentrations in the parts per million range (> 1 ppm U), we achieve lower uncertainty compared with unknowns analyzed on a multicollector and similar precision for reference materials ana-

lyzed on a quadrupole. Additionally, this study's rutile range extends to 100 times or lower uranium concentration than rutile analyzed by other instrument setups. Rutile with high uncertainty in this study is in the lower U range (< 1 ppm U).

The uncorrected U–Pb results include many discordant analyses (Fig. 3). If treated similarly to detrital zircon datasets, many analyses would be excluded by a discordance filter. However, including initially discordant data is acceptable because geologically meaningful interpretations can be made from initially discordant data when appropriate common Pb corrections are applied. U–Pb discordance in common Pb-bearing minerals is well documented in published reference materials (e.g., Chew et al., 2011, 2014). In petrochronologic applications, in situ work demonstrates that individual analyses can be nearly 100 % discordant and still interpreted confidently within the population of co-genetic grains (e.g., Poulaki et al., 2023). Although some detrital rutile U–Pb datasets are dominated by concordant analyses (e.g., Rösel et al., 2019; Kooijman et al., 2010), many detrital datasets contain analyses across the concordance spectrum, including highly discordant analyses, whose Pb-corrected dates are used in interpretations (Bracciali et al., 2013; Mark
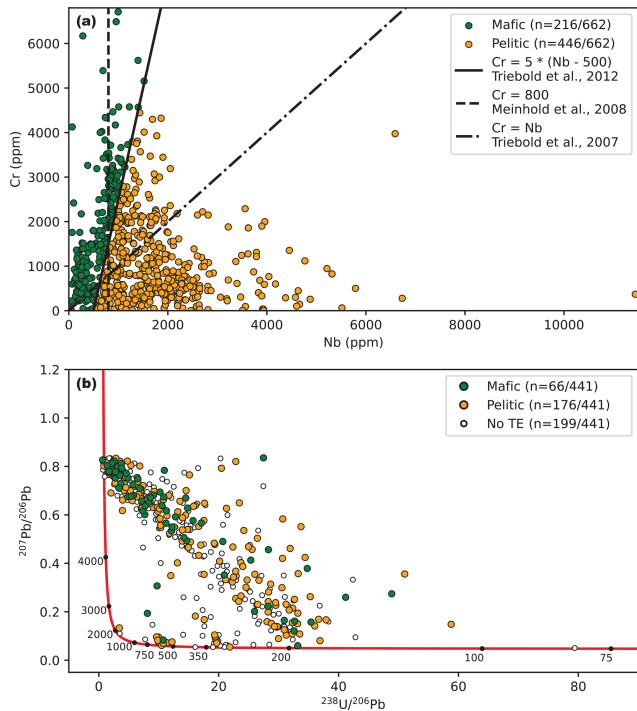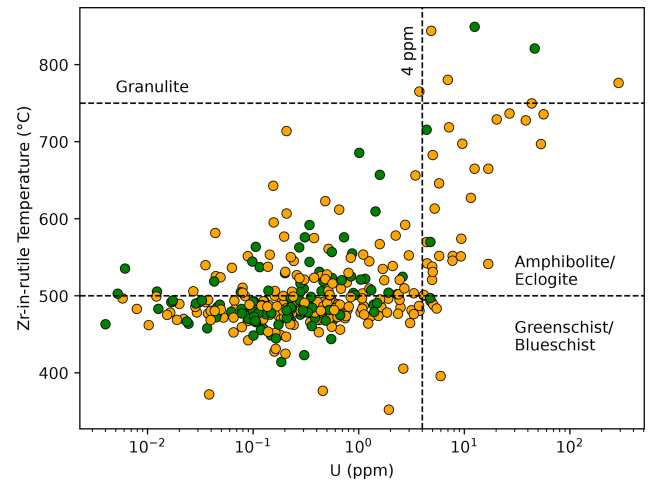
Figure 8. Zr-in-rutile temperature vs. U concentration. Mafic and pelitic discrimination is from Cr and Nb concentrations, (Fig. 7) where mafic protoliths are shown in green and pelitic protoliths in orange. The 4 ppm U line demarcates grains included or excluded by a U filter. Zr-in-rutile temperatures follow the Kohn (2020) calibration. Note that not all analyses have both U and trace element (TE) data; therefore, there are fewer grains represented in this scatterplot than in Fig. 7.

Figure 7. (a) Protolith discrimination diagram. Grains are classified as (meta)mafic and (meta)pelitic based on the Triebold et al. (2012) line, with the Triebold et al. (2007) and Meinhold et al. (2008) lines also shown. **(b)** Concordia diagram of uncorrected U–Pb circles colored by protolith classification. The power law filter is applied. Open circles represent grains with U–Pb data but no trace element (TE) data. Sample size differs between plots because not all grains have both U–Pb and trace element data.

et al., 2016; O'Sullivan et al., 2016; Govin et al., 2018; Ershova et al., 2024). Note that common ^{208}Pb and ^{207}Pb corrections force concordance so that initially discordant data are concordant after correction. We propose that the Stacey–Kramers distance is a suitable metric for quantifying discordance as it reflects U–Pb systematics (Fig. S8). However, a discordance threshold is not recommended as an exclusion criterion based on the similarity of the date distributions across concordance bins (Fig. 6). Further, most mafic-classified grains plot closer to common Pb compositions, so a discordance filter would bias results toward pelitic and high U grains (Fig. 7). For these reasons, we do not advocate filtering detrital rutile U–Pb data based on discordance.

After U–Pb data reduction, a common Pb correction and uncertainty filter were applied, which further excluded analyses. In this dataset, the ^{208}Pb and ^{207}Pb corrections produce similar date spectra (Fig. 4), and either correction method can be used. Similarly, the various uncertainty filters produce similar date distributions (Fig. 5) and we tentatively favor the power law uncertainty filter as it does not appear to alter the presence or proportion of individual age populations and because this filter excludes the fewest analyses. Future

work with large-*n* detrital datasets is needed to explore how common Pb corrections, discordance filters, and uncertainty filters influence date distributions in other datasets.

Expanding detrital rutile U–Pb applications is hindered by data rejection, as seen in this dataset and others. Caracciolo et al. (2021) attempted to present a large-*n* detrital rutile dataset in which rutile grains were identified via Raman spectroscopy. Their workflow using automated Raman is better suited for identifying polymorphs and reducing bias than the handpicking and SEM-EDS workflow used here and in many other studies. However, of the 712 detrital rutile grains analyzed by Caracciolo et al. (2021), only 347 grains remained (48 %) after their data reduction and uncertainty filtering (using a modified power law filter). Similar to our dataset, there were not enough rutile dates per sample to discuss sample-by-sample provenance interpretations (Fig. S7). Govin et al. (2018) discarded 36 % (*n* = 53/146) of detrital rutile U–Pb analyses using their date-dependent filter. Shaanan et al. (2020) present the only other detrital rutile dataset from Anatolia that does not impose a low-U filter; they discard 60 % (*n* = 97/163) of their data during discordance filtering. Together these studies illustrate that there is a formidable hurdle in trying to scale up detrital rutile U–Pb to large-*n* provenance applications.

7.2   Low-uranium rutile

Rejecting and filtering data is a common practice, whether due to abnormal signal intensity pattern, discordance, or high uncertainty. A filter based on the raw data (i.e., low U CPS) is
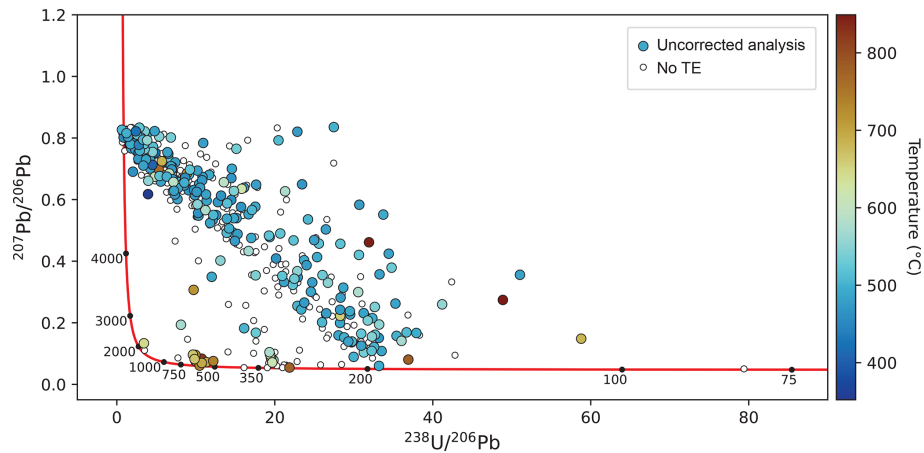
Figure 9. Uncorrected rutile U–Pb results in Tera–Wasserburg space colored by Zr-in-rutile temperature calculated from the Kohn (2020) calibration. The mode centered around 95 Ma has the highest temperatures, and modes centered around 300 and 500–650 Ma also contain high temperatures, whereas the 185 Ma mode is predominantly composed of moderate temperature grains. Open circles are rutile U–Pb analyses without trace element (TE) data. The color map is from Crameri (2018).

directly linked to counting statistics, which is a fundamental statistical limitation and not instrument type or instrument setting specific. Figure S12 shows that the main issue with the dataset presented here is the very low U and therefore Pb concentration. We demonstrate that the very, very low concentration grains have corresponding low counts and therefore high uncertainty and are therefore rejected. The rutile in this study has significantly lower U concentrations than many other studies (Fig. S12). There is a good reason to reject data with high uncertainty because they do not allow geologically significant dates to be calculated. In contrast, using a filter based on element abundance (i.e., the 4–5 ppm U threshold used in some publications) is dependent on abundance sensitivity (CPS per ppm), which depends on the instrument (laser and ICP-MS type) and instrument settings. Isotopic and elemental concentrations are calculated based on the measured count rate (i.e., counts per second), which is inherently dependent on the individual mass spectrometer and laser ablation parameters (e.g., spot size, fluence). For instruments with lower sensitivity (lower CPS per ppm), the same calculated concentration (i.e., 4–5 ppm) yields lower CPS and therefore higher analytical uncertainties than for instruments with higher sensitivity. In this way, the U threshold filter based on a calculated concentration is instrument and parameter dependent, and we therefore do not recommend this approach of screening rutile to exclude low-U-concentration analyses.

Most studies no longer impose a U threshold, but it is a regional concern in Türkiye where two of the four detrital rutile U–Pb datasets only analyze U–Pb on detrital rutile with uranium concentrations above 4–5 ppm (Okay et al., 2011; Şengün et al., 2020). The two studies that do not use a U filter analyze all detrital rutile grains (Shaanan et al., 2020; this study). In the dataset of this study, 87 % of

detrital rutile are below 4 ppm U ($n = 537/612$). The majority of detrital rutile with U > 4 ppm are classified as pelitic and generally have higher Zr contents (higher temperature), whereas low-U rutile in this study generally correlates with lower Zr contents (lower temperature) and includes the majority of mafic-classified grains (Fig. 7). Note that there are limitations to the Zr-in-rutile thermometer in mafic rocks if the equilibrium conditions are not met. Figure 10 compares U concentration with concordance and U–Pb date. Concordance does not appear to be correlated with U concentration (Fig. 10a). Comparing the date distribution for all grains with that of the groups of grains below and above 4 ppm U reveals that provenance results would be biased by excluding grains below 4 ppm U (Fig. 10c). The above 4 ppm U group has age modes at 100, 165, 315, 458, and 600 Ma (Fig. 10c pink), whereas the total date spectrum has peaks at 185, 300, 400, 450, and 600 Ma (Fig. 10c gray). The U > 4 ppm rutile group has higher-amplitude Paleozoic peaks, a minor 100 Ma peak, and a younger, lower-amplitude Mesozoic peak (165 Ma vs. 185 Ma). In summary, the U threshold filter introduces bias into the provenance results because omitting low-U rutile biases results toward metapelitic sources and higher Zr-in-rutile temperatures and shifts the prominent date modes and their amplitudes.

7.3 Source protolith and metamorphism

The Zr-in-rutile thermometer generally preserves the crystallization or recrystallization temperature. The Zr-in-rutile thermometer can become uncoupled from the U–Pb age because Pb diffusion during medium- to high-temperature metamorphic events or extended cooling periods will cause partial or complete resetting of the U–Pb system (Cherniak et al., 2007; Luvizotto and Zack, 2009; Kooijman et al., 2012;
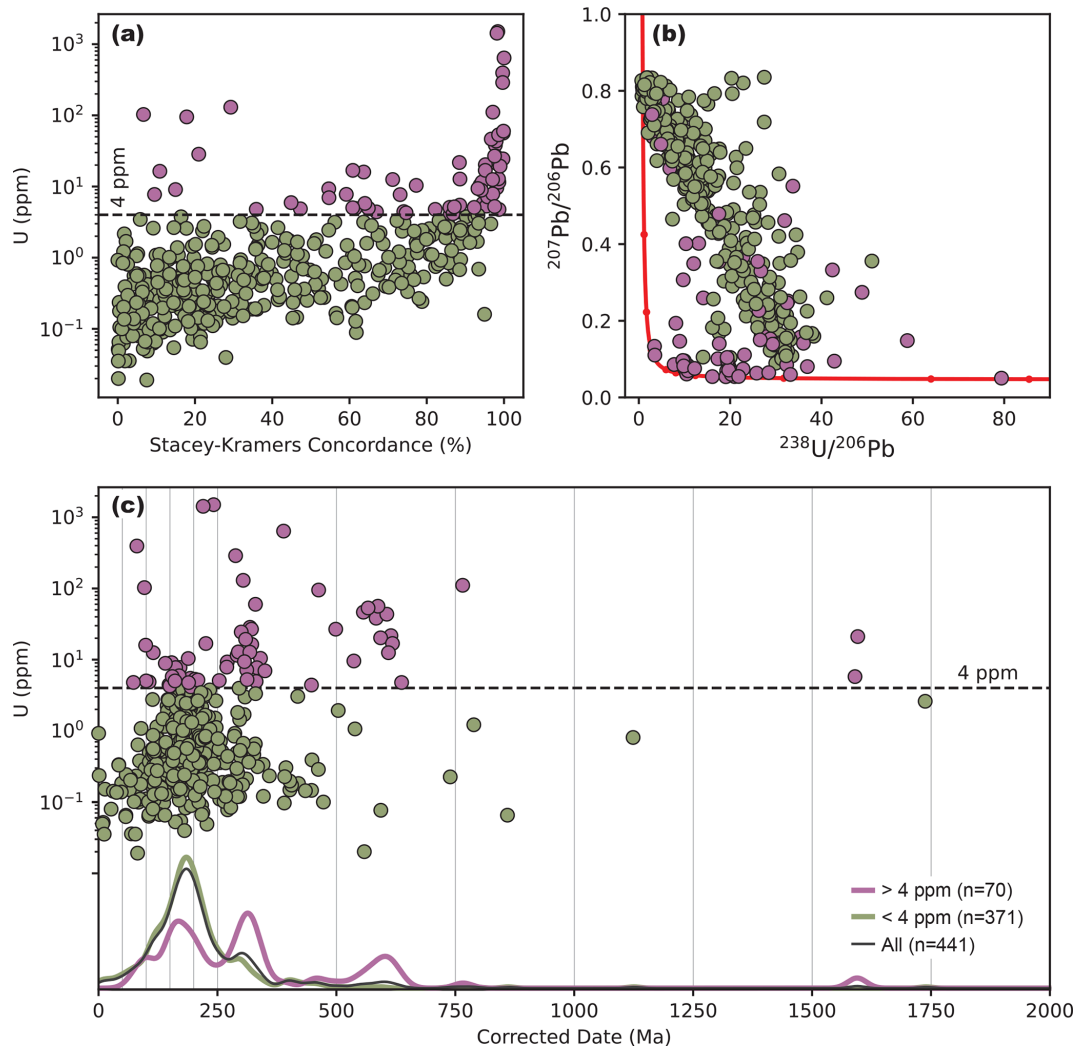
Figure 10. Comparison of detrital rutile filtering based on U concentration or concordance. **(a)** Rutile U concentration vs. percent concordance (Stacey–Kramers distance). The U threshold filter groups grains greater than and less than 4 ppm U. **(b)** Rutile U–Pb results in Tera–Wasserburg space following the color scheme in panel **(a)**. **(c)** Rutile U concentration vs. ^{207}Pb-corrected U–Pb date. The relative KDEs display the date spectra from the different U concentration groups: all analyses, above 4 ppm U, and below 4 ppm U. The power law filter is applied to all plots in the figure.

Pereira and Storey, 2023). Because temperatures calculated for the 185 Ma population are cooler than those for the older events and are not high enough to have reset the U–Pb dates, we interpret these temperatures as primary. Furthermore, partially reset dates would smear the data along concordia from the initial crystallization event age, not towards common Pb. The Zr-in-rutile temperatures and protolith classification are discussed in Sect. 8 in the context of regional provenance.

7.4 Evaluating bias in discarded U–Pb data

To evaluate the potential bias in U–Pb data reduction and processing, the detrital rutile grains with both U–Pb and trace element data are compared to those with only trace element data (U–Pb rejected and/or excluded by filter). Figure 11

gives a sense for what data are missing from the U–Pb results as well as the effects of the uncertainty filter. Note that not all detrital rutile grains have trace element data, so the subset of grains with U–Pb analyses and without trace element data cannot be considered. In the plots of protolith vs. Zr-in-rutile temperature, grains included by the power law filter (Fig. 11a) are compared to those excluded by the power law filter or without U–Pb data (Fig. 11b). Effectively this compares accepted U–Pb analyses to those rejected from unacceptable U–Pb signal patterns or high uncertainties. About 30 % of mafic-classified grains and 35 % of pelitic-classified grains are acceptable U–Pb analyses included by the power law filter (Fig. 11a). The analyses rejected by power law filtering (Fig. 11b) gave a similar temperature distribution
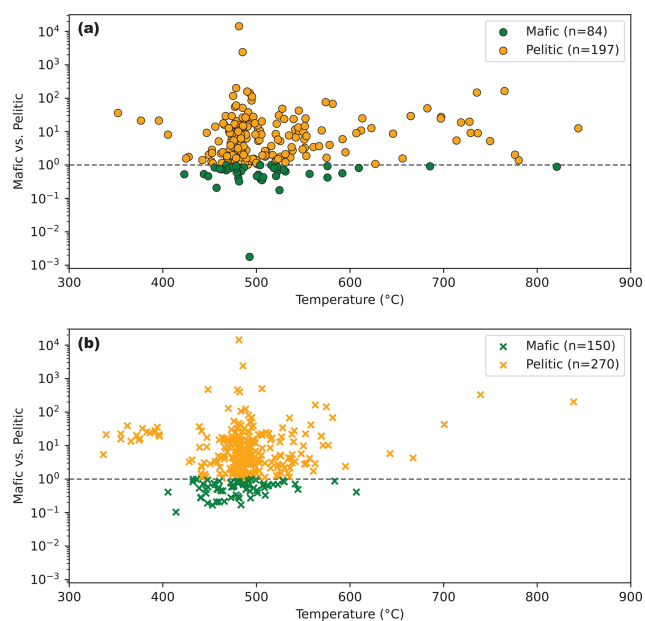
Figure 11. (a) Protolith vs. Zr-in-rutile temperature plot displays all detrital rutile analyses with trace element data included in the power law filter. Panel **(b)** shows both the detrital rutile analyses without U–Pb data and those excluded by the power law filter in **(a)**. The y axis values are the transformed distance from the mafic–pelitic discrimination line of Triebold et al. (2012) (Fig. 7).

as those included, with the majority of temperatures being from 450–550 °C. Most grains with these temperatures fall within the 185 Ma date mode (Fig. 9), potentially suggesting that the detrital rutile grains with poor U–Pb precision would have ∼ 185 Ma dates. Further, the rejected analyses group has fewer high-temperature pelitic grains (> 600 °C) and a more abundant lower-temperature pelitic population (< 400 °C). These temperature windows do not seem diagnostic of specific date populations among pelitic grains; however, about 30 % of high-temperature pelitic grains fall within the 500–650 Ma population (Fig. 9). The similarity in temperature distributions of pelitic and mafic grains between the accepted and rejected U–Pb analyses suggests that there is not significant bias in the U–Pb results due to data rejection. Consequently, we suggest that the U–Pb and trace element data can be used together to interrogate potential bias in U–Pb data rejection and filtering.

8 Anatolian sedimentary provenance

Sedimentary provenance is interpreted from all detrital rutile dates together, rather than by sample, due to the small number of analyses in each sample (see Fig. S7 for individual sample results). The detrital rutile results are displayed along with detrital zircon dates from the same Upper Cretaceous to Eocene units in the Central Sakarya and Sarıcakaya basins (Fig. 12; data from Campbell, 2017; Ocakoğlu et al.,

2018; Mueller et al., 2019, 2022; Okay and Kylander-Clark, 2022). The detrital zircon and rutile provenance results are discussed together from youngest to oldest date population. The rutile grains that (poorly) define the ca. 90 Ma population (Fig. 12) include some of the highest Zr-in-rutile temperatures (Fig. 9). The zircon record has abundant Late Cretaceous and Eocene populations (Fig. 12) associated with magmatic flare-ups during Alpine orogeny-related subduction and syn-collisional magmatism, respectively (Harris et al., 1994; Kasapoğlu et al., 2016; Yildiz et al., 2015; Ocakoğlu et al., 2018; Mueller et al., 2022; Campbell et al., 2023). The lower plate Anatolide–Tauride terrane underwent HP/LT blueschist facies metamorphism that generally decreases in age from Late Cretaceous in the north to early Eocene in the south (Sherlock et al., 1999; Okay and Kelley, 1994; Candan et al., 2005; Pourteau et al., 2016). However, the samples are from sedimentary basins on the Pontides (Fig. 12) and the detrital zircon record indicates no sediment transport across the suture zone between from the Anatolide–Tauride terranes to the Pontides in the latest Cretaceous (Okay and Kylander-Clark, 2022). Thus, we interpret the 90 Ma rutile population as either igneous or metamorphic rutile derived from Late Cretaceous magmatism and associated contact metamorphism on the Pontides.

The 185 Ma peak includes the lowest Zr-in-rutile temperatures (∼ 450–550 °C; Fig. 9), mafic and pelitic sources (Fig. 7), and predominantly low-U rutile (Fig. 10). The age, lithology, and temperature findings support a Karakaya Complex sediment source. The Permian–Triassic Karakaya Complex contains intra-oceanic basalts and forearc deposits that were metamorphosed to blueschist and epidote–amphibolite facies ($340–550 \pm 50$ °C; Okay et al., 2002; Federici et al., 2010) during the Triassic Cimmerian event. The rutile U–Pb dates interpreted as Karakaya Complex (broad 185 Ma peak) are younger than existing Karakaya Complex phengite, glaucophane, and barroisite Ar–Ar cooling dates (∼ 200–215 Ma: Okay et al., 2002; Federici et al., 2010; Şengör et al., 1984). The closure temperature windows for rutile U–Pb and phengite Ar–Ar overlap, with Pb in rutile extending to lower temperature than Ar in phengitic white mica (Itaya, 2020; Marty Grove, personal communication, 2024). The younger rutile dates likely indicate protracted cooling because extended time spent in the partial retention zone would cause variable Pb loss that could lead to a younger rutile U–Pb dates than any actual heating event and/or a spread in ages (broad peak). This 185 Ma population is not prominent in the detrital zircon spectra. Detrital zircons from Karakaya Complex units have age modes at ca. 235, 315, and 400 Ma and are interpreted as sediment input to the forearc from the Pontides Triassic magmatic arc, oceanic plateau, or spreading center (e.g., Okay et al., 2015); Variscan granitoids; and crystalline basement (Ustaömer et al., 2016).

The Carboniferous peaks in the zircon and rutile record correspond to a ∼ 330–340 Ma pulse of high-T metamorphism and ∼ 290–320 Ma magmatism in the Pontides dur-
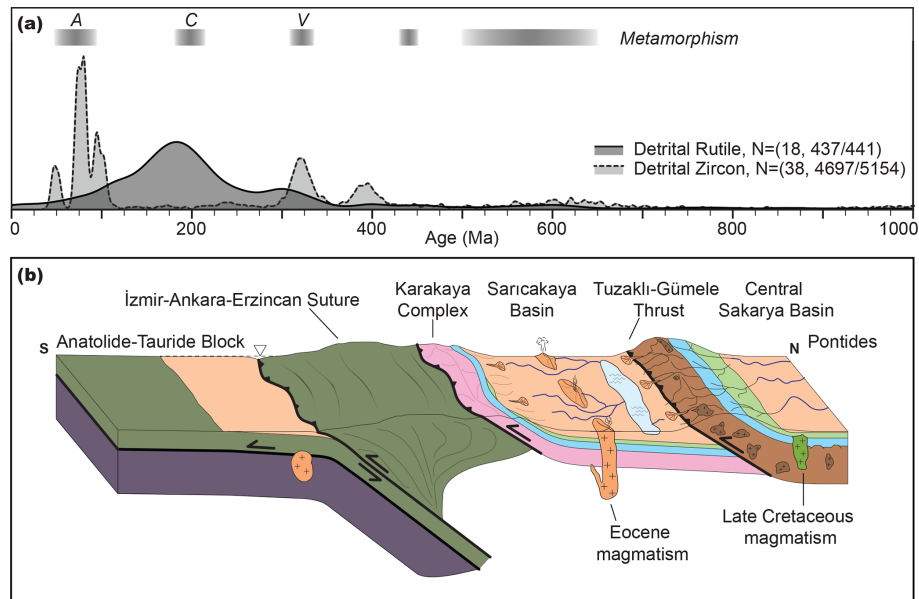
Figure 12. (a) Kernel density estimate of all detrital rutile dates (^{207}Pb-corrected, power law uncertainty-filtered) shown alongside a compilation of all published detrital zircon ages from Upper Cretaceous to Eocene strata in Central Sakarya and Sarıcakaya basins. Gray bars depict periods of metamorphism in western Anatolia. **(b)** Schematic reconstruction of northwestern Anatolia in the Eocene during continental collision (after Mueller et al., 2019). The main sources of sediment to the basins were the Karakaya Complex exposed in the suture zone, Pontides crystalline basement exposed along the Tuzaklı–Gümele Thrust, Cretaceous–Eocene igneous units, and recycled sedimentary units. A stands for Alpine metamorphism, C stands for Cimmerian metamorphism, and V stands for Variscan metamorphism.

ing the Variscan orogeny (Topuz et al., 2007, 2020; Ustaömer et al., 2012, 2013). Variscan-aged detrital rutiles are found in Jurassic sandstones in the Central Sakarya Basin and interpreted as derived from either primary Pontide basement or recycled sedimentary sources (Şengün et al., 2020). The Pontide basement units crop out along the Tuzaklı–Gümele Thrust fault that partitions the two sedimentary basins (Fig. 12b). Therefore, the Variscan-aged detrital rutile could be derived from primary basement sources or recycled Jurassic sedimentary units. The Pontides crystalline basement contains scarce Devonian (380–400 Ma) and Silurian (420–440 Ma) metaigneous rocks, which are exposed in the hanging wall of the Tuzaklı–Gümele Thrust (Topuz et al., 2020). The paucity of this age population in the rutile record could be due to the scarcity of outcrops, small sample size, dilution during sediment recycling, or overprinting by the Carboniferous high-temperature event. Late Ordovician–Early Silurian metamorphism associated with the accretion of the Istanbul–Moesia–Scythian Platform (Okay et al., 2006) is not prominent in the detrital rutile record, which could suggest the absence of major south-directed sediment transport across the Pontides (i.e., from the Istanbul Zone to Sakarya Zone across Intra-Pontide ocean or suture) during the Late Cretaceous to Eocene. Lastly, the 500–650 Ma Pan-African detrital rutile ages align with the detrital zircon age spectra. Gondwana-derived terranes are characterized by Neoproterozoic–Cambrian plutonism and metamorphism

from the Pan-African–Cadomian orogeny, which is not well documented in Anatolia (Okay et al., 2006). Grains of this age could be sourced from the Pontides basement or recycled from sedimentary units (Ustaömer et al., 2012; Mueller et al., 2019). However, if the grains of this age were first cycle from crystalline basement sources, we would expect them to have reset, younger U–Pb dates reflective of younger metamorphic reheating events. However, by this reasoning, the presence of 500–650 Ma dates indicates that these grains must have been unaffected by the younger high-T events (i.e., Variscan, Cimmerian, and Alpine metamorphism). In order to have escaped metamorphic reheating, the grains had to have been already eroded from the crystalline basement and deposited in sedimentary units. Therefore, we interpret the 500–650 Ma grains as polycyclic grains derived from recycled sedimentary units. Together, the detrital zircon and rutile age spectra demonstrate that, from the Late Cretaceous to Eocene, sediment was routed to the Central Sakarya and Sarıcakaya basins from syn-depositional magmatic centers, the Karakaya Complex within the suture zone, the Pontides crystalline basement, and recycled sedimentary units (Fig. 12).

9   Conclusions

This work provides a systematic exploration of the data reduction and processing workflows for detrital rutile U–Pb geochronology using a new dataset from the Central Sakarya

and Sarıcakaya basins in Anatolia. Provenance interpretations are made from combining U–Pb dates and trace element geochemistry. The results have several implications for navigating workflows and interpretations in common Pb-bearing detrital minerals.

1. Natural datasets can be complex. While attempting a large-*n* provenance study, a significant number of analyses were discarded due to unacceptable U–Pb signal intensity and stability, namely low U, low Pb, and inclusions. This hurdle is evidently not unique to this dataset and should always be reported in detrital rutile U–Pb geochronology. Advances are needed to determine the best path forward, such as analyzing more grains for achieving large-*n* detrital rutile U–Pb datasets and more rigorous data reporting and standardizing metrics used for evaluating "acceptable" U–Pb analyses. We recommend that the criteria for data rejection be explicitly discussed in all detrital rutile studies.

2. We provide a method for evaluating the potential bias in U–Pb data rejection and filtering by comparing the detrital rutile grains with both U–Pb and trace element data to those with only trace element data. The rejected and filtered out grains have a similar trace element distribution in terms of Zr-in-rutile temperature and mafic–pelitic classification to those with acceptable U–Pb analyses, suggesting there is not significant bias from U–Pb data rejection and filtering.

3. The ^{208}Pb and ^{207}Pb correction methods produce similar age spectra and do not change the final provenance interpretations. Similarly, the uncertainty filters – based on U–Pb ratio uncertainty and corrected date uncertainty – produce similar date spectra. The power law uncertainty filter is preferred because it does not alter the date distribution and includes the most grains.

4. There has not been an agreed upon metric to quantify discordance in common Pb minerals. We evaluate various distance metrics (Sect. S3) and recommend the Stacey-Kramers distance as a suitable metric for quantifying discordance. However, because reliable interpretations can be made from analyses with significant proportions of common Pb, we do not recommend applying a discordance filter to common Pb detrital minerals.

5. In some labs and geographic locations, only rutile above a certain uranium concentration (i.e., 4–5 ppm U) are analyzed for U–Pb. We demonstrate that excluding low-U rutile biases provenance interpretations toward grains with pelitic protoliths, higher Zr-in-rutile temperatures, and higher concordance, and changes the overall date distribution, especially the amplitude of date peaks.

6. A significant challenge in provenance work is pinpointing the signature of sediment recycling. Here we use paired U–Pb dates and Zr-in-rutile temperatures to identify polycyclic detrital rutile grains. The recycled grains preserve U–Pb dates that indicate that they escaped younger metamorphic reheating events of the crystalline basement by already being eroded and deposited in sedimentary units. In this way, detrital rutile petrochronology can address problems of sediment recycling.

7. The data processing workflows used here are provided as code in Jupyter notebooks that can be used by future studies. The code includes common Pb corrections, uncertainty filters, discordance calculations, and trace element plots. The provided code is one path forward to achieving the required documentation and unification of data reduction approaches.

Additional sample information is included in the supplemental text of the data repository (https://doi.org/10.17605/OSF.IO/A4YE5, Mueller et al., 2023).

References

Açıkalın, S., Ocakoğlu, F., Yýlmaz, Ý. Ö., Vonhof, H., Hakyemez, A., and Smit, J.: Stable isotopes and geochemistry of a Campanian–Maastrichtian pelagic succession, Mudurnu–Göynük Basin, NW Turkey: Implications for palaeoceanography, palaeoclimate and sea-level fluctuations, Palaeogeogr. Palaeocl., 441, 453–466, https://doi.org/10.1016/j.palaeo.2015.10.005, 2016.

Aksay, A., Pehlivan, S¸., Gedik, I., Býlginer, E., Duru, M., Akbas¸, B., and Altun, I.: Geologic map of Turkey (Zonguldak, Scale 1 : 500 000), Maden Tetkik ve Arma Genel Müdürlüğü, Ankara, Turkey, 2002.

Andersen, T.: Correction of common lead in U-Pb analyses that do not report ^{204}Pb, Chem. Geol., 192, 59–79, https://doi.org/10.1016/S0009-2541(02)00195-X, 2002.

Angiboust, S. and Harlov, D.: Ilmenite breakdown and rutile-titanite stability in metagranitoids: Natural observations and experimental results, Am. Mineral., 102, 1696–1708, https://doi.org/10.2138/am-2017-6064, 2017.

Apen, F. E., Rudnick, R. L., Cottle, J. M., Kylander-Clark, A. R. C., Blondes, M. S., Piccoli, P. M., and Seward, G.: Four-dimensional thermal evolution of the East African Orogen: accessory phase petrochronology of crustal profiles through the Tanzanian Craton and Mozambique Belt, northeastern Tanzania, Contrib. Mineral. Petrol., 175, 97, https://doi.org/10.1007/s00410-020-01737-6, 2020.

Blackburn, T. J., Bowring, S. A., Perron, J. T., Mahan, K. H., Dudas, F. O., and Barnhart, K. R.: An Exhumation History of Continents over Billion-Year Time Scales, Science, 335, 73–76, https://doi.org/10.1126/science.1213496, 2012.

Blum, M. and Pecha, M.: Mid-Cretaceous to Paleocene North American drainage reorganization from detrital zircons, Geology, 42, 607–610, https://doi.org/10.1130/G35513.1, 2014.

Bracciali, L.: Coupled Zircon-Rutile U-Pb Chronology: LA ICP-MS Dating, Geological Significance and Applications to Sediment Provenance in the Eastern Himalayan-Indo-Burman Region, Geosciences, 9, 467, https://doi.org/10.3390/geosciences9110467, 2019.

Bracciali, L., Parrish, R. R., Horstwood, M. S. A., Condon, D. J., and Najman, Y.: UPb LA-(MC)-ICP-MS dating of rutile: New reference materials and applications to sedimentary provenance, Chem. Geol., 347, 82–101, https://doi.org/10.1016/j.chemgeo.2013.03.013, 2013.

Bracciali, L., Najman, Y., Parrish, R. R., Akhter, S. H., and Millar, I.: The Brahmaputra tale of tectonics and erosion: Early Miocene river capture in the Eastern Himalaya, Earth Planet. Sc. Lett., 415, 25–37, https://doi.org/10.1016/j.epsl.2015.01.022, 2015.

Campbell, C. F.: Tectonic Evolution of the Izmir-Ankara Suture Zone in Northwest Turkey using Zircon U-Pb Geochronology and Zircon Lu-Hf Isotopic Tracers, M.S., University of Kansas, United States–Kansas, 99 pp., 2017.

Campbell, C. F., Mueller, M. A., Taylor, M. H., Ocakoğlu, F., Möller, A., Métais, G., Coster, P. M. C., Beard, K. C., and Licht, A.: The Geodynamic Implications of Passive Margin Subduction in Northwest Turkey, Geochem. Geophys. Geosyst., 24, e2022GC010481, https://doi.org/10.1029/2022GC010481, 2023.

Candan, O., Çetinkaplan, M., Oberhänsli, R., Rimmelé, G., and Akal, C.: Alpine high-P/low-T metamorphism of the Afyon Zone and implications for the metamorphic evolution of Western Anatolia, Turkey, Lithos, 84, 102–124, https://doi.org/10.1016/j.lithos.2005.02.005, 2005.

Caracciolo, L., Ravidà, D. C. G., Chew, D., Janßen, M., Lünsdorf, N. K., Heins, W. A., Stephan, T., and Stollhofen, H.: Reconstructing environmental signals across the Permian-Triassic boundary in the SE Germanic Basin: A Quantitative Provenance Analysis (QPA) approach, Glob. Planet. Change, 206, 103631, https://doi.org/10.1016/j.gloplacha.2021.103631, 2021.

Carrapa, B.: Resolving tectonic problems by dating detrital minerals, Geology, 38, 191–192, https://doi.org/10.1130/focus022010.1, 2010.

Cave, B. J., Stepanov, A. S., Craw, D., Large, R. R., Halpin, J. A., and Thompson, J.: RELEASE OF TRACE ELEMENTS THROUGH THE SUB-GREENSCHIST FACIES BREAKDOWN OF DETRITAL RUTILE TO METAMORPHIC TITANITE IN THE OTAGO SCHIST, NEW ZEALAND, Can. Mineral., 53, 379–400, https://doi.org/10.3749/canmin.1400097, 2015.

Cherniak, D. J.: Pb diffusion in rutile, Contrib. Mineral. Petrol., 139, 198–207, https://doi.org/10.1007/PL00007671, 2000.

Cherniak, D. J., Manchester, J., and Watson, E. B.: Zr and Hf diffusion in rutile, Earth Planet. Sc. Lett., 261, 267–279, https://doi.org/10.1016/j.epsl.2007.06.027, 2007.

Chew, D., O'Sullivan, G., Caracciolo, L., Mark, C., and Tyrrell, S.: Sourcing the sand: Accessory mineral fertility, analytical and other biases in detrital U-Pb provenance analysis, Earth-Sci. Rev., 202, 103093, https://doi.org/10.1016/j.earscirev.2020.103093, 2020.

Chew, D. M., Sylvester, P. J., and Tubrett, M. N.: U–Pb and Th–Pb dating of apatite by LA-ICPMS, Chem. Geol., 280, 200–216, https://doi.org/10.1016/j.chemgeo.2010.11.010, 2011.

Chew, D. M., Petrus, J. A., and Kamber, B. S.: U-Pb LA-ICPMS dating using accessory mineral standards with variable common Pb, Chem. Geol., 363, 185–199, https://doi.org/10.1016/j.chemgeo.2013.11.006, 2014.

Clark, D. J., Hensen, B. J., and Kinny, P. D.: Geochronological constraints for a two-stage history of the Albany–Fraser Orogen, Western Australia, Precambrian Res., 102, 155–183, https://doi.org/10.1016/S0301-9268(00)00063-2, 2000.

Clift, P. D., Hodges, K. V., Heslop, D., Hannigan, R., Van Long, H., and Calves, G.: Correlation of Himalayan exhumation rates and Asian monsoon intensity, Nat. Geosci., 1, 875–880, https://doi.org/10.1038/ngeo351, 2008.

Clift, P. D., Mark, C., Alizai, A., Khan, H., and Jan, M. Q.: Detrital U–Pb rutile and zircon data show Indus River sediment dominantly eroded from East Karakoram, not Nanga Parbat, Earth Planet. Sc. Lett., 600, 117873, https://doi.org/10.1016/j.epsl.2022.117873, 2022.

Compston, W., Williams, I. S., and Meyer, C.: U-Pb geochronology of zircons from lunar breccia 73217 using a sensitive high mass-resolution ion microprobe, J. Geophys. Res.-Sol. Ea., 89, B525–B534, https://doi.org/10.1029/JB089iS02p0B525, 1984.

Crameri, F.: Scientific colour maps: perceptually uniform and colour-vision deficiency friendly, Zenodo [code], https://doi.org/10.5281/zenodo.1243862, 2018.

Davis, W. J., Canil, D., MacKenzie, J. M., and Carbno, G. B.: Petrology and U–Pb geochronology of lower crustal xenoliths and the development of a craton, Slave Province, Canada, Lithos, 71, 541–573, https://doi.org/10.1016/S0024-4937(03)00130-0, 2003.

Dickinson, W. R. and Suczek, C. A.: Plate Tectonics and Sandstone Compositions, AAPG Bull., 63, 2164–2182, 1979.

Dodson, M. H.: Closure Temperature in Cooling Geochronological and Petrological Systems, Contrib. Mineral. Petrol., 40, 259–274, 1973.

Ershova, V., Prokopiev, A., and Stockli, D.: Provenance of Detrital Rutiles from the Triassic–Jurassic Sandstones in Franz Josef Land (Barents Sea Region, Russian High Arctic): U-Pb Ages and Trace Element Geochemistry, Geosciences, 14, 41, https://doi.org/10.3390/geosciences14020041, 2024.

Ersoy, E. Y., Akal, C., Genç, S¸. C., Candan, O., Palmer, M. R., Preleviæ, D., Uysal, Ý., and Mertz-Kraus, R.: U-Pb zircon geochronology of the Paleogene – Neogene volcanism in the NW Anatolia: Its implications for the Late Mesozoic-Cenozoic geodynamic evolution of the Aegean, Tectonophysics, 717, 284–301, https://doi.org/10.1016/j.tecto.2017.08.016, 2017.

Ersoy, E. Y., Akal, C., Palmer, M. R., and Mertz-Kraus, R.: U-Pb dating of arc to post-collisional magmatic events in northwestern Anatolia: The Eocene Granitoids in NW Anatolia revisited, J. Asian Earth Sci. X, 9, 100148, https://doi.org/10.1016/j.jaesx.2023.100148, 2023.

Ewing, T. A.: Hf isotope analysis and U-Pb geochronology of rutile: technique development and application to a lower crustal section (Ivrea-Verbano Zone, Italy), PhD thesis from Australian National University, https://doi.org/10.25911/5d74e68841e8d, 2011.

Ewing, T. A., Rubatto, D., Beltrando, M., and Hermann, J.: Constraints on the thermal evolution of the Adriatic margin during Jurassic continental break-up: U–Pb dating of rutile from the Ivrea–Verbano Zone, Italy, Contrib. Mineral. Petrol., 169, 44, https://doi.org/10.1007/s00410-015-1135-6, 2015.

Faure, G.: Principles of Isotope Geology, 2nd Edition., Wiley & Sons, Inc., 608 pp., 1986.

Federici, I., Cavazza, W., Okay, A. I., Beyssac, O., Zattin, M., Corrado, S., and Dellisanti, F.: Thermal Evolution of the Permo-Triassic Karakaya Subduction-accretion Complex between the Biga Peninsula and the Tokat Massif (Anatolia), Turk. J. Earth Sci., 19, 409–429, https://doi.org/10.3906/yer-0910-39, 2010.

Ferry, J. M. and Watson, E. B.: New thermodynamic models and revised calibrations for the Ti-in-zircon and Zr-in-rutile thermometers, Contrib. Mineral. Petrol., 154, 429–437, https://doi.org/10.1007/s00410-007-0201-0, 2007.

Flowers, R. M., Bowring, S. A., Tulloch, A. J., and Klepeis, K. A.: Tempo of burial and exhumation within the deep roots of a magmatic arc, Fiordland, New Zealand, Geology, 33, 17–20, https://doi.org/10.1130/G21010.1, 2005.

Foley, S. F., Barth, M. G., and Jenner, G. A.: Rutile/melt partition coefficients for trace elements and an assessment of the influence of rutile on the trace element characteristics of subduction zone magmas, Geochim. Cosmochim. Ac., 64, 933–938, https://doi.org/10.1016/S0016-7037(99)00355-5, 2000.

Garzanti, E. and Andò, S.: Heavy Mineral Concentration in Modern Sands: Implications for Provenance Interpretation, in: Developments in Sedimentology, vol. 58, edited by: Mange, M. A. and

Wright, D. T., Elsevier, 517–545, https://doi.org/10.1016/S0070-4571(07)58020-9, 2007.

Garzanti, E., Doglioni, C., Vezzoli, G., and Ando, S.: Orogenic belts and orogenic sediment provenance, J. Geol., 115, 315–334, 2007.

Gaschnig, R. M.: Benefits of a Multiproxy Approach to Detrital Mineral Provenance Analysis: An Example from the Merrimack River, New England, USA, Geochem. Geophys. Geosystems, 20, 1557–1573, https://doi.org/10.1029/2018GC008005, 2019.

Gazzi, P.: On the Heavy Mineral Zones in the Geosyncline Series. Recent Studies in the Northern Apennines, Italy, J. Sediment. Petrol., 35, 109–115, https://doi.org/10.1306/74D71203-2B21-11D7-8648000102C1865D, 1965.

Gehrels, G.: Detrital Zircon U-Pb Geochronology: Current Methods and New Opportunities, in: Tectonics of Sedimentary Basins, John Wiley & Sons, Ltd, 45–62, https://doi.org/10.1002/9781444347166.ch2, 2011.

Gehrels, G.: Detrital Zircon U-Pb Geochronology Applied to Tectonics, Annu. Rev. Earth Planet. Sci., 42, 127–149, https://doi.org/10.1146/annurev-earth-050212-124012, 2014.

Gehrels, G. E., Valencia, V. A., and Ruiz, J.: Enhanced precision, accuracy, efficiency, and spatial resolution of U-Pb ages by laser ablation–multicollector–inductively coupled plasma–mass spectrometry, Geochem. Geophys. Geosyst., 9, Q03017, https://doi.org/10.1029/2007GC001805, 2008.

Göncüoğlu, M. C., Turhan, N., Şentürk, K., Özcan, A., Uysal, S., and Yaliniz, M. K.: A Geotraverse Across Northwestern Turkey: Tectonic Units of the Central Sakarya Region and their Tectonic Evolution, Geol. Soc. Lond. Spec. Publ., 173, 139–161, https://doi.org/10.1144/GSL.SP.2000.173.01.06, 2000.

Govin, G., Najman, Y., Copley, A., Millar, I., van der Beek, P., Huyghe, P., Grujic, D., and Davenport, J.: Timing and mechanism of the rise of the Shillong Plateau in the Himalayan foreland, Geology, 46, 279–282, https://doi.org/10.1130/G39864.1, 2018.

Guo, R., Hu, X., Garzanti, E., Lai, W., Yan, B., and Mark, C.: How faithfully do the geochronological and geochemical signatures of detrital zircon, titanite, rutile and monazite record magmatic and metamorphic events? A case study from the Himalaya and Tibet, Earth-Sci. Rev., 201, 103082, https://doi.org/10.1016/j.earscirev.2020.103082, 2020.

Harris, N. B. W., Kelley, S., and Okay, A. I.: Post-collisional magmatism and tectonics in northwest Anatolia, Contrib. Mineral. Petrol., 117, 241–252, 1994.

Hart, E., Storey, C., Bruand, E., Schertl, H.-P., and Alexander, B. D.: Mineral inclusions in rutile: A novel recorder of HP-UHP metamorphism, Earth Planet. Sc. Lett., 446, 137–148, https://doi.org/10.1016/j.epsl.2016.04.035, 2016.

Hart, E., Storey, C., Harley, S. L., and Fowler, M.: A window into the lower crust: Trace element systematics and the occurrence of inclusions/intergrowths in granulite-facies rutile, Gondwana Res., 59, 76–86, https://doi.org/10.1016/j.gr.2018.02.021, 2018.

Hietpas, J., Samson, S., Moecher, D., and Schmitt, A. K.: Recovering tectonic events from the sedimentary record: Detrital monazite plays in high fidelity, Geology, 38, 167–170, https://doi.org/10.1130/G30265.1, 2010.

Hietpas, J., Samson, S., Moecher, D., and Chakraborty, S.: Enhancing tectonic and provenance information from detrital zircon studies: assessing terrane-scale sampling and grain-scale characterization, J. Geol. Soc., 168, 309–318, https://doi.org/10.1144/0016-76492009-163, 2011.

Hubert, J. F.: Analysis of heavy-mineral assemblages, in: Procedures in sedimentary petrology, edited by: Carver, R. E., New York: Wiley-Interscience, 453–478, 1971.

Itaya, T.: K–Ar phengite geochronology of $HP - -UHP$ metamorphic rocks – An in–depth review, J. Mineral. Petrol. Sci., 115, 44–58, https://doi.org/10.2465/jmps.190123, 2020.

Jenkins, K., Goemann, K., Belousov, I., Morissette, M., and Danyushevsky, L.: Investigation of the Ablation Behaviour of Andradite-Grossular Garnets and Rutile with Implications for U-Pb Geochronology, Geostand. Geoanalytical Res., 47, 267–295, https://doi.org/10.1111/ggr.12478, 2023.

Jochum, K. P., Wilson, S. A., Abouchami, W., Amini, M., Chmeleff, J., Eisenhauer, A., Hegner, E., Iaccheri, L. M., Kieffer, B., Krause, J., McDonough, W. F., Mertz-Kraus, R., Raczek, I., Rudnick, R. L., Scholz, D., Steinhoefel, G., Stoll, B., Stracke, A., Tonarini, S., Weis, D., Weis, U., and Woodhead, J. D.: GSD-1G and MPI-DING Reference Glasses for In Situ and Bulk Isotopic Determination, Geostand. Geoanalytical Res., 35, 193–226, https://doi.org/10.1111/j.1751-908X.2010.00114.x, 2011.

Kasapoğlu, B., Ersoy, Y. E., Uysal, Ý., Palmer, M. R., Zack, T., Koralay, E. O., and Karlsson, A.: The petrology of Paleogene volcanism in the Central Sakarya, Nallýhan Region: Implications for the initiation and evolution of post-collisional, slab break-off-related magmatic activity, Lithos, 246–247, 81–98, https://doi.org/10.1016/j.lithos.2015.12.024, 2016.

Kellett, D. A., Weller, O. M., Zagorevski, A., and Regis, D.: A petrochronological approach for the detrital record: Tracking mm-sized eclogite clasts in the northern Canadian Cordillera, Earth Planet. Sc. Lett., 494, 23–31, https://doi.org/10.1016/j.epsl.2018.04.036, 2018.

Keskin, M. and Tüysüz, O.: Stratigraphy, petrogenesis and geodynamic setting of Late Cretaceous volcanism on the SW margin of the Black Sea, Turkey, Geol. Soc. Lond. Spec. Publ., 464, 95–130, https://doi.org/10.1144/SP464.5, 2018.

Klemme, S., Blundy, J. D., and Wood, B. J.: Experimental constraints on major and trace element partitioning during partial melting of eclogite, Geochim. Cosmochim. Ac., 66, 3109–3123, https://doi.org/10.1016/S0016-7037(02)00859-1, 2002.

Kohn, M. J.: A refined zirconium-in-rutile thermometer, Am. Mineral., 105, 963–971, https://doi.org/10.2138/am-2020-7091, 2020.

Kohn, M. J. and Kelly, N. M.: Petrology and Geochronology of Metamorphic Zircon, in: Geophysical Monograph Series, edited by: Moser, D. E., Corfu, F., Darling, J. R., Reddy, S. M., and Tait, K., John Wiley & Sons, Inc., Hoboken, NJ, USA, 35–61, https://doi.org/10.1002/9781119227250.ch2, 2017.

Kooijman, E., Mezger, K., and Berndt, J.: Constraints on the U–Pb systematics of metamorphic rutile from in situ LA-ICP-MS analysis, Earth Planet. Sc. Lett., 293, 321–330, https://doi.org/10.1016/j.epsl.2010.02.047, 2010.

Kooijman, E., Smit, M. A., Mezger, K., and Berndt, J.: Trace element systematics in granulite facies rutile: implications for Zr geothermometry and provenance studies, J. Metamorph. Geol., 30, 397–412, https://doi.org/10.1111/j.1525-1314.2012.00972.x, 2012.

Kylander-Clark, A. R. C.: Slow subduction and exhumation of a thick ultrahigh -pressure terrane: Western Gneiss Region, Nor-

way, Ph.D., University of California, Santa Barbara, United States, California, 121 pp., 2008.

Kylander-Clark, A. R. C., Hacker, B. R., and Mattinson, J. M.: Slow exhumation of UHP terranes: Titanite and rutile ages of the Western Gneiss Region, Norway, Earth Planet. Sc. Lett., 272, 531–540, https://doi.org/10.1016/j.epsl.2008.05.019, 2008.

Lippert, P. G.: Detrital U-Pb geochronology provenance analyses: case studies in the Greater Green River Basin, Wyoming, and the Book Cliffs, Utah, Thesis, University of Kansas, 2014.

Ludwig, K. R.: On the Treatment of Concordant Uranium-Lead Ages, Geochim. Cosmochim. Ac., 62, 665–676, https://doi.org/10.1016/S0016-7037(98)00059-3, 1998.

Luvizotto, G. L. and Zack, T.: Nb and Zr behavior in rutile during high-grade metamorphism and retrogression: An example from the Ivrea–Verbano Zone, Chem. Geol., 261, 303–317, https://doi.org/10.1016/j.chemgeo.2008.07.023, 2009.

Luvizotto, G. L., Zack, T., Meyer, H. P., Ludwig, T., Triebold, S., Kronz, A., Münker, C., Stockli, D. F., Prowatke, S., Klemme, S., Jacob, D. E., and von Eynatten, H.: Rutile crystals as potential trace element and isotope mineral standards for microanalysis, Chem. Geol., 261, 346–369, https://doi.org/10.1016/j.chemgeo.2008.04.012, 2009.

Mark, C., Cogné, N., and Chew, D.: Tracking exhumation and drainage divide migration of the Western Alps: A test of the apatite U-Pb thermochronometer as a detrital provenance tool, GSA Bull., 128, 1439–1460, https://doi.org/10.1130/B31351.1, 2016.

McLean, N. M., Bowring, J. F., and Bowring, S. A.: An algorithm for U-Pb isotope dilution data reduction and uncertainty propagation, Geochem. Geophys. Geosyst., 12, 1–26, https://doi.org/10.1029/2010GC003478, 2011.

Meinhold, G.: Rutile and its applications in earth sciences, Earth-Sci. Rev., 102, 1–28, https://doi.org/10.1016/j.earscirev.2010.06.001, 2010.

Meinhold, G., Anders, B., Kostopoulos, D., and Reischmann, T.: Rutile chemistry and thermometry as provenance indicator: An example from Chios Island, Greece, Sediment. Geol., 203, 98–111, https://doi.org/10.1016/j.sedgeo.2007.11.004, 2008.

Meinhold, G., Morton, A. C., Fanning, C. M., and Whitham, A. G.: U–Pb SHRIMP ages of detrital granulite-facies rutiles: further constraints on provenance of Jurassic sandstones on the Norwegian margin, Geol. Mag., 148, 473–480, https://doi.org/10.1017/S0016756810000877, 2010.

Mezger, K., Hanson, G. N., and Bohlen, S. R.: High-precision UPb ages of metamorphic rutile: application to the cooling history of high-grade terranes, Earth Planet. Sc. Lett., 96, 106–118, https://doi.org/10.1016/0012-821X(89)90126-X, 1989.

Moecher, D., Hietpas, J., Samson, S., and Chakraborty, S.: Insights into southern Appalachian tectonics from ages of detrital monazite and zircon in modern alluvium, Geosphere, 7, 494–512, https://doi.org/10.1130/GES00615.1, 2011.

Möller, A., Mezger, K., and Schenk, V.: U–Pb dating of metamorphic minerals: Pan-African metamorphism and prolonged slow cooling of high pressure granulites in Tanzania, East Africa, Precambrian Res., 104, 123–146, https://doi.org/10.1016/S0301-9268(00)00086-3, 2000.

Morton, A. and Yaxley, G.: Detrital apatite geochemistry and its application in provenance studies, Geol. Soc. Am. Spec. Pap., 420, 319–344, https://doi.org/10.1130/2006.2420(19), 2007.

Morton, A. C.: Heavy minerals in provenance studies, in: Provenance of Arenites, edited by: Zuffa, G. G., Reidel, Dordrecht, 249–277, 1985.

Mueller, M., Licht, A., Möller, A., Condit, C., Fosdick, J. C., Ocakoğlu, F., and Campbell, C.: Supplemental data for: Navigating the complexity of detrital rutile provenance: Methodological insights from the Neotethys Orogen in Anatolia, OSFHome [data set], https://doi.org/10.17605/OSF.IO/A4YE5, 2023.

Mueller, M. A.: 16SKY04, SESAR [sample], https://doi.org/10.58052/IEMUE0017, 2021a.

Mueller, M. A.: 16SKY09, SESAR [sample], https://doi.org/10.58052/IEMUE0019, 2021b.

Mueller, M. A.: 16SKY23, SESAR [sample], https://doi.org/10.58052/IEMUE001H, 2021c.

Mueller, M. A.: 16SKY26, SESAR [sample], https://doi.org/10.58052/IEMUE001K, 2021d.

Mueller, M. A.: 16SKY37, SESAR [sample], https://doi.org/10.58052/IEMUE001Q, 2021e.

Mueller, M. A.: 16SKY42, SESAR [sample], https://doi.org/10.58052/IEMUE001T, 2021f.

Mueller, M. A.: 16SKY50, SESAR [sample], https://doi.org/10.58052/IEMUE001W, 2021g.

Mueller, M. A.: 17OZK05, SESAR [sample], https://doi.org/10.58052/IEMUE001Z, 2021h.

Mueller, M. A.: 18DMN01, SESAR [sample], https://doi.org/10.58052/IEMUE0005, 2022a.

Mueller, M. A.: 18NAL12, SESAR [sample], https://doi.org/10.58052/IEMUE000J, 2022b.

Mueller, M. A.: 18TK01, SESAR [sample], https://doi.org/10.58052/IEMUE0001, 2022c.

Mueller, M. A.: 18KIZ01, SESAR [sample], https://doi.org/10.58052/IEMUE000C, 2022d.

Mueller, M. A.: 18YEN05, SESAR [sample], https://doi.org/10.58052/IEMUE000D, 2022e.

Mueller, M. A.: 18TB01, SESAR [sample], https://doi.org/10.58052/IEMUE000F, 2022f.

Mueller, M. A.: 18TBTG, SESAR [sample], https://doi.org/10.58052/IEMUE000G, 2022g.

Mueller, M. A.: 18YP03, SESAR [sample], https://doi.org/10.58052/IEMUE000K, 2022h.

Mueller, M. A.: 17MGB02, SESAR [sample], https://doi.org/10.58052/IEMUE0007, 2022i.

Mueller, M. A.: 18YEN01, SESAR [sample], https://doi.org/10.58052/IEMUE0008, 2022j.

Mueller, M. A.: 18YEN04, SESAR [sample], https://doi.org/10.58052/IEMUE0009, 2022k.

Mueller, M. A.: 18HAL01, SESAR [sample], https://doi.org/10.58052/IEMUE000A, 2022l.

Mueller, M. A.: mmueller13/Detrital-UPb-and-TE: v0.2, Zenodo [code], https://doi.org/10.5281/zenodo.10636728, 2024.

Mueller, M. A., Licht, A., Campbell, C., Ocakoğlu, F., Taylor, M. H., Burch, L., Ugrai, T., Kaya, M., Kurtoğlu, B., Coster, P. M. C., Métais, G., and Beard, K. C.: Collision Chronology Along the Ýzmir-Ankara-Erzincan Suture Zone: Insights From the Sarýcakaya Basin, Western Anatolia, Tectonics, 38, 3652–3674, https://doi.org/10.1029/2019TC005683, 2019.

Mueller, M. A., Licht, A., Campbell, C., Ocakoğlu, F., Akşịt, G. G., Métais, G., Coster, P. M. C., Beard, K. C., and Taylor, M. H.: Sedimentary Provenance From the Evolving Forearc-to-Foreland

Central Sakarya Basin, Western Anatolia Reveals Multi-Phase Intercontinental Collision, Geochem. Geophys. Geosyst., 23, e2021GC010232, https://doi.org/10.1029/2021GC010232, 2022.

Ocakoğlu, F., Hakyemez, A., Açıkalın, S., Özkan Altýner, S., Büyükmeriç, Y., Licht, A., Demircan, H., Sąfak, Ü., Yýldýz, A., Yilmaz, Ý. Ö., Wagreich, M., and Campbell, C.: Chronology of subduction and collision along the Ýzmir-Ankara suture in Western Anatolia: records from the Central Sakarya Basin, Int. Geol. Rev., 1–26, https://doi.org/10.1080/00206814.2018.1507009, 2018.

Odlum, M. L., Stockli, D. F., Capaldi, T. N., Thomson, K. D., Clark, J., Puigdefàbregas, C., and Fildani, A.: Tectonic and sediment provenance evolution of the South Eastern Pyrenean foreland basins during rift margin inversion and orogenic uplift, Tectonophysics, 765, 226–248, https://doi.org/10.1016/j.tecto.2019.05.008, 2019.

Odlum, M. L., Capaldi, T. N., Thomson, K. D., and Stockli, D. F.: Tracking cycles of Phanerozoic opening and closing of ocean basins using detrital rutile and zircon geochronology and geochemistry, Geology, https://doi.org/10.1130/G51826.1, 2024.

Okay, A., Satir, M., and Siebel, W.: Pre-Alpide Palaeozoic and Mesozoic Orogenic Events in the Eastern Mediterranean Region, Geol. Soc. Lond. Mem., 32, 389–405, https://doi.org/10.1144/GSL.MEM.2006.032.01.23, 2006.

Okay, A. I. and Göncüoglu, M. C.: The Karakaya Complex: A Review of Data and Concepts, Turk. J. Earth Sci., 13, 77–95, 2004.

Okay, A. I. and Kelley, S. P.: Tectonic setting, petrology and geochronology of jadeite + glaucophane and chloritoid + glaucophane schists from north-west Turkey, J. Metamorph. Geol., 12, 455–466, https://doi.org/10.1111/j.1525-1314.1994.tb00035.x, 1994.

Okay, A. I. and Kylander-Clark, A. R. C.: No sediment transport across the Tethys ocean during the latest Cretaceous: detrital zircon record from the Pontides and the Anatolide–Tauride Block, Int. J. Earth Sci., https://doi.org/10.1007/s00531-022-02275-1, 2022.

Okay, A. I., Monod, O., and Monié, P.: Triassic blueschists and eclogites from northwest Turkey: vestiges of the Paleo-Tethyan subduction, Lithos, 64, 155–178, https://doi.org/10.1016/S0024-4937(02)00200-1, 2002.

Okay, A. I., Altiner, D., and Kiliç, A. M.: Triassic limestone, turbidites and serpentinite – the Cimmeride orogeny in the Central Pontides, Geol. Mag., 152, 460–479, https://doi.org/10.1017/S0016756814000429, 2015.

Okay, A. I., Sunal, G., Sherlock, S., Kylander-Clark, A. R. C., and Özcan, E.: Ýzmir-Ankara Suture as a Triassic to Cretaceous Plate Boundary – Data From Central Anatolia, Tectonics, 39, e2019TC005849, https://doi.org/10.1029/2019TC005849, 2020.

Okay, N., Zack, T., Okay, A. I., and Barth, M.: Sinistral transport along the Trans-European Suture Zone: detrital zircon–rutile geochronology and sandstone petrography from the Carboniferous flysch of the Pontides, Geol. Mag., 148, 380–403, https://doi.org/10.1017/S0016756810000804, 2011.

O'Sullivan, G., Chew, D., Kenny, G., Henrichs, I., and Mulligan, D.: The trace element composition of apatite and its application to detrital provenance studies, Earth-Sci. Rev., 201, 103044, https://doi.org/10.1016/j.earscirev.2019.103044, 2020.

O'Sullivan, G. J., Chew, D. M., and Samson, S. D.: Detecting magma-poor orogens in the detrital record, Geology, 44, 871–874, https://doi.org/10.1130/G38245.1, 2016.

Paterson, S. R. and Ducea, M. N.: Arc Magmatic Tempos: Gathering the Evidence, Elements, 11, 91–98, https://doi.org/10.2113/gselements.11.2.91, 2015.

Paton, C., Hellstrom, J., Paul, B., Woodhead, J., and Hergt, J.: Iolite: Freeware for the visualisation and processing of mass spectrometric data, J. Anal. At. Spectrom., 26, 2508, https://doi.org/10.1039/c1ja10172b, 2011.

Pereira, I. and Storey, C. D.: Detrital rutile: Records of the deep crust, ores and fluids, Lithos, 107010, https://doi.org/10.1016/j.lithos.2022.107010, 2023.

Pereira, I., Storey, C. D., Strachan, R. A., Bento dos Santos, T., and Darling, J. R.: Detrital rutile ages can deduce the tectonic setting of sedimentary basins, Earth Planet. Sc. Lett., 537, 116193, https://doi.org/10.1016/j.epsl.2020.116193, 2020.

Pereira, I., Storey, C. D., Darling, J. R., Moreira, H., Strachan, R. A., and Cawood, P. A.: Detrital rutile tracks the first appearance of subduction zone low T/P paired metamorphism in the Palaeoproterozoic, Earth Planet. Sc. Lett., 570, 117069, https://doi.org/10.1016/j.epsl.2021.117069, 2021.

Pickett, E. A. and Robertson, A. H. F.: Formation of the Late Palaeozoic–Early Mesozoic Karakaya Complex and related ophiolites in NW Turkey by Palaeotethyan subduction–accretion, J. Geol. Soc., 153, 995–1009, https://doi.org/10.1144/gsjgs.153.6.0995, 1996.

Plavsa, D., Reddy, S. M., Agangi, A., Clark, C., Kylander-Clark, A., and Tiddy, C. J.: Microstructural, trace element and geochronological characterization of TiO_2 polymorphs and implications for mineral exploration, Chem. Geol., 476, 130–149, https://doi.org/10.1016/j.chemgeo.2017.11.011, 2018.

Poulaki, E. M., Stockli, D. F., and Shuck, B. D.: Pre-Subduction Architecture Controls Coherent Underplating During Subduction and Exhumation (Nevado-Filábride Complex, Southern Spain), Geochem. Geophys. Geosyst., 24, e2022GC010802, https://doi.org/10.1029/2022GC010802, 2023.

Pourteau, A., Oberhänsli, R., Candan, O., Barrier, E., and Vrielynck, B.: Neotethyan closure history of western Anatolia: a geodynamic discussion, Int. J. Earth Sci., 105, 203–224, https://doi.org/10.1007/s00531-015-1226-7, 2016.

Rösel, D., Boger, S. D., Möller, A., Gaitzsch, B., Barth, M., Oalmann, J., and Zack, T.: Indo-Antarctic derived detritus on the northern margin of Gondwana: evidence for continental-scale sediment transport, Terra Nova, 26, 64–71, https://doi.org/10.1111/ter.12070, 2014.

Rösel, D., Zack, T., and Möller, A.: Interpretation and significance of combined trace element and U–Pb isotopic data of detrital rutile: a case study from late Ordovician sedimentary rocks of Saxo-Thuringia, Germany, Int. J. Earth Sci., 108, 1–25, https://doi.org/10.1007/s00531-018-1643-5, 2019.

Rudnick, R., Barth, M., Horn, I., and McDonough, W. F.: Rutile-Bearing Refractory Eclogites: Missing Link Between Continents and Depleted Mantle, Science, 287, 278–281, https://doi.org/10.1126/science.287.5451.278, 2000.

Schärer, U., Krogh, T. E., and Gower, C. F.: Age and evolution of the Grenville Province in eastern Labrador from U-Pb systematics in accessory minerals, Contrib. Mineral. Petrol., 94, 438–451, https://doi.org/10.1007/BF00376337, 1986.

Schmitz, M. D. and Bowring, S. A.: Constraints on the thermal evolution of continental lithosphere from U-Pb accessory mineral thermochronometry of lower crustal xenoliths, southern Africa, Contrib. Mineral. Petrol., 144, 592–618, https://doi.org/10.1007/s00410-002-0419-9, 2003.

Schoene, B.: U–Th–Pb Geochronology, in: Treatise on Geochemistry, Elsevier, 341–378, https://doi.org/10.1016/B978-0-08-095975-7.00310-7, 2014.

Şengör, A. M. C. and Yilmaz, Y.: Tethyan evolution of turkey: a plate tectonic approach, Tectonophysics, 75, 181–241, 1981.

Şengör, A. M. C., Yýlmaz, Y., and Sungurlu, O.: Tectonics of the Mediterranean Cimmerides: nature and evolution of the western termination of Palaeo-Tethys, Geol. Soc. Lond. Spec. Publ., 17, 77–112, https://doi.org/10.1144/GSL.SP.1984.017.01.04, 1984.

Şengün, F., Zack, T., and Dunkl, I.: Provenance of detrital rutiles from the Jurassic sandstones in the Central Sakarya Zone, NW Turkey: U-Pb ages and trace element geochemistry, Geochemistry, 80, 125667, https://doi.org/10.1016/j.chemer.2020.125667, 2020.

Shaanan, U., Avigad, D., Morag, N., Güngör, T., and Gerdes, A.: Drainage response to Arabia–Eurasia collision: Insights from provenance examination of the Cyprian Kythrea flysch (Eastern Mediterranean Basin), Basin Res., 33, 26–47, https://doi.org/10.1111/bre.12452, 2020.

Sharman, G. R., Sharman, J. P., and Sylvester, Z.: detritalPy: A Python-based toolset for visualizing and analysing detrital geo-thermochronologic data, Depositional Rec., 4, 202–215, https://doi.org/10.1002/dep2.45, 2018.

Sherlock, S., Kelley, S., Inger, S., Harris, N., and Okay, A.: 40Ar-39Ar and Rb-Sr geochronology of high-pressure metamorphism and exhumation history of the Tavsanli Zone, NW Turkey, Contrib. Mineral. Petrol., 137, 46–58, https://doi.org/10.1007/PL00013777, 1999.

Simonetti, A., Heaman, L. M., Hartlaub, R. P., Creaser, R. A., MacHattie, T. G., and Böhm, C.: U–Pb zircon dating by laser ablation-MC-ICP-MS using a new multiple ion counting Faraday collector array, J. Anal. At. Spectrom., 20, 677–686, https://doi.org/10.1039/B504465K, 2005.

Smye, A. J. and Stockli, D. F.: Rutile U–Pb age depth profiling: A continuous record of lithospheric thermal evolution, Earth Planet. Sc. Lett., 408, 171–182, https://doi.org/10.1016/j.epsl.2014.10.013, 2014.

Smye, A. J., Marsh, J. H., Vermeesch, P., Garber, J. M., and Stockli, D. F.: Applications and limitations of U-Pb thermochronology to middle and lower crustal thermal histories, Chem. Geol., 494, 1–18, https://doi.org/10.1016/j.chemgeo.2018.07.003, 2018.

Stacey, J. S. and Kramers, J. D.: Approximation of terrestrial lead isotope evolution by a two-stage model, Earth Planet. Sc. Lett., 26, 207–221, https://doi.org/10.1016/0012-821X(75)90088-6, 1975.

Steiger, R. H. and Jäger, E.: Subcommission on geochronology: Convention on the use of decay constants in geo- and cosmochronology, Earth Planet. Sc. Lett., 36, 359–362, https://doi.org/10.1016/0012-821X(77)90060-7, 1977.

Storey, C. D., Jeffries, T. E., and Smith, M.: Common lead-corrected laser ablation ICP–MS U–Pb systematics and geochronology of titanite, Chem. Geol., 227, 37–52, https://doi.org/10.1016/j.chemgeo.2005.09.003, 2006.

Storey, C. D., Smith, M. P., and Jeffries, T. E.: In situ LA-ICP-MS U–Pb dating of metavolcanics of Norrbotten, Sweden: Records of extended geological histories in complex titanite grains, Chem. Geol., 240, 163–181, https://doi.org/10.1016/j.chemgeo.2007.02.004, 2007.

Sundell, K. E., George, S. W. M., Carrapa, B., Gehrels, G. E., Ducea, M. N., Saylor, J. E., and Pepper, M.: Crustal Thickening of the Northern Central Andean Plateau Inferred From Trace Elements in Zircon, Geophys. Res. Lett., 49, e2021GL096443, https://doi.org/10.1029/2021GL096443, 2022.

Tang, M., Ji, W.-Q., Chu, X., Wu, A., and Chen, C.: Reconstructing crustal thickness evolution from europium anomalies in detrital zircons, Geology, 49, 76–80, https://doi.org/10.1130/G47745.1, 2020.

Templ, M., Hron, K., and Filzmoser, P.: robCompositions: An R-package for Robust Statistical Analysis of Compositional Data, in: Compositional Data Analysis, John Wiley & Sons, Ltd, 341–355, https://doi.org/10.1002/9781119976462.ch25, 2011.

Tera, F. and Wasserburg, G. J.: U-Th-Pb systematics in three Apollo 14 basalts and the problem of initial Pb in lunar rocks, Earth Planet. Sc. Lett., 14, 281–304, https://doi.org/10.1016/0012-821X(72)90128-8, 1972.

Tomkins, H. S., Powell, R., and Ellis, D. J.: The pressure dependence of the zirconium-in-rutile thermometer, J. Metamorph. Geol., 25, 703–713, https://doi.org/10.1111/j.1525-1314.2007.00724.x, 2007.

Topuz, G., Altherr, R., Schwarz, W. H., Dokuz, A., and Meyer, H.-P.: Variscan amphibolite-facies rocks from the Kurtoğlu metamorphic complex (Gümüşhane area, Eastern Pontides, Turkey), Int. J. Earth Sci., 96, 861–873, https://doi.org/10.1007/s00531-006-0138-y, 2007.

Topuz, G., Candan, O., Okay, A. I., von Quadt, A., Othman, M., Zack, T., and Wang, J.: Silurian anorogenic basic and acidic magmatism in Northwest Turkey: Implications for the opening of the Paleo-Tethys, Lithos, 356–357, 105302, https://doi.org/10.1016/j.lithos.2019.105302, 2020.

Triebold, S., von Eynatten, H., Luvizotto, G. L., and Zack, T.: Deducing source rock lithology from detrital rutile geochemistry: An example from the Erzgebirge, Germany, Chem. Geol., 244, 421–436, https://doi.org/10.1016/j.chemgeo.2007.06.033, 2007.

Triebold, S., Luvizotto, G. L., Tolosana-Delgado, R., Zack, T., and von Eynatten, H.: Discrimination of TiO2 polymorphs in sedimentary and metamorphic rocks, Contrib. Mineral. Petrol., 161, 581–596, https://doi.org/10.1007/s00410-010-0551-x, 2011.

Triebold, S., von Eynatten, H., and Zack, T.: A recipe for the use of rutile in sedimentary provenance analysis, Sediment. Geol., 282, 268–275, https://doi.org/10.1016/j.sedgeo.2012.09.008, 2012.

Ustaömer, P., Ustaömer, T., and Robertson, Alastair. H. F.: Ion Probe U-Pb Dating of the Central Sakarya Basement: A peri-Gondwana Terrane Intruded by Late Lower Carboniferous Subduction/Collision-related Granitic Rocks, Turk. J. Earth Sci., 21, 905–932, https://doi.org/10.3906/yer-1103-1, 2012.

Ustaömer, T., Robertson, A. H. F., Ustaömer, P. A., Gerdes, A., and Peytcheva, I.: Constraints on Variscan and Cimmerian magmatism and metamorphism in the Pontides (Yusufeli–Artvin area), NE Turkey from U–Pb dating and granite geochemistry, Geol. Soc. Lond. Spec. Publ., 372, 49–74, https://doi.org/10.1144/SP372.13, 2013.

Ustaömer, T., Ustaömer, P., Robertson, A. H. F., and Gerdes, A.: Implications of U–Pb and Lu–Hf isotopic analysis of detrital zircons for the depositional age, provenance and tectonic setting of the Permian–Triassic Palaeotethyan Karakaya Complex, NW Turkey, Int. J. Earth Sci., 105, 7–38, https://doi.org/10.1007/s00531-015-1225-8, 2016.

Vermeesch, P.: Unifying the U–Pb and Th–Pb methods: joint isochron regression and common Pb correction, Geochronology, 2, 119–131, https://doi.org/10.5194/gchron-2-119-2020, 2020.

Vermeesch, P.: On the treatment of discordant detrital zircon U–Pb data, Geochronology, 3, 247–257, https://doi.org/10.5194/gchron-3-247-2021, 2021.

Vry, J. K. and Baker, J. A.: LA-MC-ICPMS Pb–Pb dating of rutile from slowly cooled granulites: Confirmation of the high closure temperature for Pb diffusion in rutile, Geochim. Cosmochim. Ac., 70, 1807–1820, https://doi.org/10.1016/j.gca.2005.12.006, 2006.

Watson, E. B., Wark, D. A., and Thomas, J. B.: Crystallization thermometers for zircon and rutile, Contrib. Mineral. Petrol., 151, 413, https://doi.org/10.1007/s00410-006-0068-5, 2006.

Williams, I. S.: U-Th-Pb Geochronology by Ion Microprobe, in: Applications of Microanalytical Techniques to Understanding Mineralizing Processes, Society of Economic Geologists, 1–35, https://doi.org/10.5382/Rev.07.01, 1997.

Xiong, X. L., Adam, J., and Green, T. H.: Rutile stability and rutile/melt HFSE partitioning during partial melting of hydrous basalt: Implications for TTG genesis, Chem. Geol., 218, 339–359, https://doi.org/10.1016/j.chemgeo.2005.01.014, 2005.

Yildiz, A., Kibici, Y., Bağci, M., Dumlupunar, Ý., Kocabas, C., and Aritan, A. E.: Petrogenesis of the post-collisional Eocene volcanic rocks from the Central Sakarya Zone (Northwestern Anatolia, Turkey): Implications for source characteristics, magma evolution, and tectonic setting, Arab. J. Geosci., 8, 11239–11260, https://doi.org/10.1007/s12517-015-1991-4, 2015.

Zack, T. and Kooijman, E.: Petrochronology and Geochronology of Rutile, Rev. Mineral. Geochem., 83, 443–467, 2017.

Zack, T., von Eynatten, H., and Kronz, A.: Rutile geochemistry and its potential use in quantitative provenance studies, Sediment. Geol., 171, 37–58, https://doi.org/10.1016/j.sedgeo.2004.05.009, 2004a.

Zack, T., Moraes, R., and Kronz, A.: Temperature dependence of Zr in rutile: empirical calibration of a rutile thermometer, Contrib. Mineral. Petrol., 148, 471–488, https://doi.org/10.1007/s00410-004-0617-8, 2004b.

Zack, T., Stockli, D. F., Luvizotto, G. L., Barth, M. G., Belousova, E., Wolfe, M. R., and Hinton, R. W.: In situ U–Pb rutile dating by LA-ICP-MS: 208Pb correction and prospects for geological applications, Contrib. Mineral. Petrol., 162, 515–530, https://doi.org/10.1007/s00410-011-0609-4, 2011.

Zoleikhaei, Y., Mulder, J. A., and Cawood, P. A.: Integrated detrital rutile and zircon provenance reveals multiple sources for Cambrian sandstones in North Gondwana, Earth-Sci. Rev., 213, 103462, https://doi.org/10.1016/j.earscirev.2020.103462, 2021.